Taylor & Francis
Taylor & Francis Group

Geomechanics and Geoengineering
An International Journal

ISSN: (Print) (Online) Journal homepage: https://www.tandfonline.com/loi/tgeo20

Dynamic behaviour of a piled raft resting on saturated Kasai River sand

Raj Banerjee, Rana Chattaraj, Aniruddha Sengupta & Y. M. Parulekar

To cite this article: Raj Banerjee, Rana Chattaraj, Aniruddha Sengupta & Y. M. Parulekar (2022) Dynamic behaviour of a piled raft resting on saturated Kasai River sand, Geomechanics and Geoengineering, 17:4, 1023-1055, DOI: 10.1080/17486025.2021.1912403

To link to this article: https://doi.org/10.1080/17486025.2021.1912403

Published online: 20 May 2021.

GEOMECHANICS AND GEOENGINEERING
2022, VOL. 17, NO. 4, 1023–1055
https://doi.org/10.1080/17486025.2021.1912403

ARTICLE

Dynamic behaviour of a piled raft resting on saturated Kasai River sand

Raj Banerjee [a], Rana Chattaraj [b], Aniruddha Sengupta [c] and Y. M. Parulekar [a]

[a]Structural and Seismic Engineering Section, Bhabha Atomic Research Center, Mumbai, India; [b]Civil Engineering Department, Kalinga Institute of Technology, Bhubneswar, India; [c]Civil Engineering Department, Indian Institute of Technology, Kharagpur, India

ABSTRACT

The present work intends to calibrate the cyclic triaxial test and validate the 1-g shake table test of piled raft on saturated Kasai River sand. The outcome of the cyclic tests on Kasai river sand is already reported in the literature, but the present paper attempts to identify and explain the failure modes of the cyclic triaxial test as well as to numerically calibrate the experimental data(s) for relative density of 40% and 60%. For numerical validation and calibration, a bounding surface plasticity model is used. The calibrated parameters obtained from the element tests are used for validation of 1-g shake table test of piled raft resting on saturated sand. The numerical predictions are in good agreement with the experimental observations (in terms of acceleration, pore pressure). In addition, the effect of superstructure loading on piled raft is investigated in terms of variation of pore pressure (or effective stress) near and away from the structure and mechanism for vertical settlement of piled raft is identified. The relevant parameters related to seismic design of piled raft are identified and design guidelines in terms of strength and serviceability has been proposed.

ARTICLE HISTORY

Received 11 February 2020
Accepted 30 March 2021

KEYWORDS

Liquefaction; cyclic triaxial test; piled raft; Kasai River sand

1. Introduction

The prediction of liquefaction and resulting displacements is a major concern for structures located in the regions of moderate to high seismicity (Byrne *et al.* (2004)). It is observed that the presence of even thin layers of liquefiable soil will lead to significant deformation which can cause serious damage (Dashti *et al.* (2009a, 2009b)). It is noteworthy that the additional safety in the design of superstructure is not of any help in the event of liquefaction of foundation soil during an earthquake (Mittal *et al.* (2004)). The laboratory and the field observations clearly indicate that the soil types which are susceptible to the liquefaction are clean sand, silty sand or sandy silt and gravels (Erten and Maher (1995), Amini and Qi (2000), Salgado *et al.* (2000), Polito and Martin (2001), Yamamuro and Covert (2001), Thevanayagam and Martin (2002)). Horikoshi *et al.* (2003b) conducted several dynamic centrifuge tests on piled raft foundation resting on cohesion less soil and also examined the effect of the rigidity of pile head connection on the behaviour of piled raft. Nakai *et al.* (2004) conducted dynamic centrifuge model tests on piled raft and pile group in order to compare the seismic performance between the two of them. Knappett and Madabhushi (2008, 2009a, 2009b) conducted numerous dynamic centrifuge tests in order to understand the variation of axial load on ach pile in a piled foundations resting on liquefiable soil. Stringer and Madabhushi (2013a, 2013b) performed several dynamic centrifuge experiments on pile group and piled raft to evaluate the distribution of axial loads along the pile during earthquakes in liquefiable soil. Sahraeian *et al.* (2017, 2018) studied the seismic behaviour of oil tank on piled raft foundation resting on dry and liquefiable sand through dynamic centrifuge model experiments. Some other works related to the behaviour of deep foundations (mainly piled raft or pile group) on liquefiable soil have been reported by Dash and Bhattacharya (2015), Fallahzadeh *et al.* (2019), Tasiopoulou *et al.* (2013), Unsever *et al.* (2017), Wang *et al.* (2019). These studies on piled rafts have been found to mitigate liquefaction and reduce the severity of damage on a superstructure due to soil liquefaction.

The present study hinges upon the findings of the previous literature(s) on the responses of deep foundation on saturated soil. With the increase in the number of important structures, such as, railway bridges, residential colonies, etc., built on the banks of Kasai River, the need for understanding the behaviour of deep foundations resting on liquefiable strata is of prime importance. Also the proximity of a number of faults, like Pingla fault, Garhmayna Khanda Ghosh Fault and Eocene Hinge Zone, to the Kasai River (Dasgupta *et al.* (2000)) has caused mild seismic shaking a number of

CONTACT Raj Banerjee rajbanerji90@gmail.com

times in the recent past. The area under consideration comes under the Seismic Zone III in the seismic zonation map of India (IS 1893 (2002)). The Peak Ground Acceleration (PGA) predicted by GSHAP Model for the area is between 0.2 and 0.3 g. Thus the seismic vulnerability assessment of the structures located along Kasai River is very much required to minimise the potential loss during a seismic event.

As a part to mitigate a liquefaction event, Chattaraj and Sengupta (2016) has proposed the dynamic characteristics of Kasai River sand experimentally using resonant column and cyclic triaxial test. They have proposed variation of G_{max} with confining pressure and relative density, variation of G/G_{max} and damping ratio with shear strain, CRR with number of cycles for different relative densities, etc. Due to the lack of field measurements from the actual events, small-scaled model tests provide an efficient way to reduce the uncertainties associated with the behaviour of soil and structure in the prototype condition (Hushmand *et al.* (1988)). Although it is acknowledged that the stress and the deformation of the soil cannot be exactly represented in the small-scale models due to its size limitation (Ueng *et al.* (2005)).In this study, an attempt is made to study the behaviour of a piled raft foundation on Kasai River sand subjected to seismic shaking in low confining stress(s) (in a 1-g gravitational field) using the dynamic tests conducted on the river sand. The element tests on Kasai River sand are numerically simulated using a well known bounding surface plasticity model, PM4 sand (Boulanger and Ziotopoulou (2015)) to find out the calibrated model parameters. After the calibration of the model parameters, the model tests conducted on the shake table with a piled raft foundation is simulated numerically in 1-g environment. The numerical predictions are found to be in good agreement with the experimental observations (in terms of acceleration, pore pressure). In addition, the effect of superstructure loading on piled raft is investigated in terms of variation of pore pressure (or effective stress) near and away from the structure, identification of mechanism for vertical settlement of piled raft. The relevant parameters related to the seismic piled raft design are identified and a design guideline in terms of strength and serviceability has been proposed which may help a designer to come up with an efficient design for a piled raft foundation with due consideration for the foundation soil liquefaction.

In absence of such element test data (cyclic triaxial, resonant column) for prediction of the prototype results, the authors propose a 'practice-oriented approach' in which if the soil N-value ($(N_1)_{60}$) is known (or may be back calculated from relative density), the liquefaction triggering correlation by Idriss and Boulanger (2008) can be used to find a target cyclic resistance ratio correspond to $(N_1)_{60}$. Next, with this target cyclic resistance set, undrained cyclic simple shear element simulations will be done with the model parameters adjusted such that liquefaction occurs in 15 cycles.

2. Soil properties

Local uniform grained sand (Kasai River sand) is used in this study. The grain size distribution of the sand is shown in Figure 1. It is classified as poorly graded sand (SP), according to the Unified Soil Classification System (USCS). Its grain size distribution as well as the range of gradation for liquefiable sand given by (Xenaki and Athanasopoulos (2003)) is shown in Figure 1. As may be seen from the figure, the saturated Kasai River sand under dynamic loading condition is susceptible to liquefaction. The specific gravity of the sand is 2.7. The maximum dry unit weight $\gamma_{d(max)}$ is 18.00 kN/m^3, and the minimum dry unit weight $\gamma_{d(min)}$ is 14.03 kN/m^3. The uniformity coefficient (C_u) and coefficient of curvature (C_c) of the sand are found to be 2.84 and 0.87, respectively. Drained shear tests are performed on the sand to find its shear strength parameters. The details of the test is given in Banerjee *et al.* (2019) from which the effective cohesion (c') and the effective angle of friction (φ') are found to be 0.0 kPa and 32°, respectively. In this study, a relationship (of shear wave velocity (or shear modulus) with depth (increase in the confining pressure) and changes in relative density of soil) has been

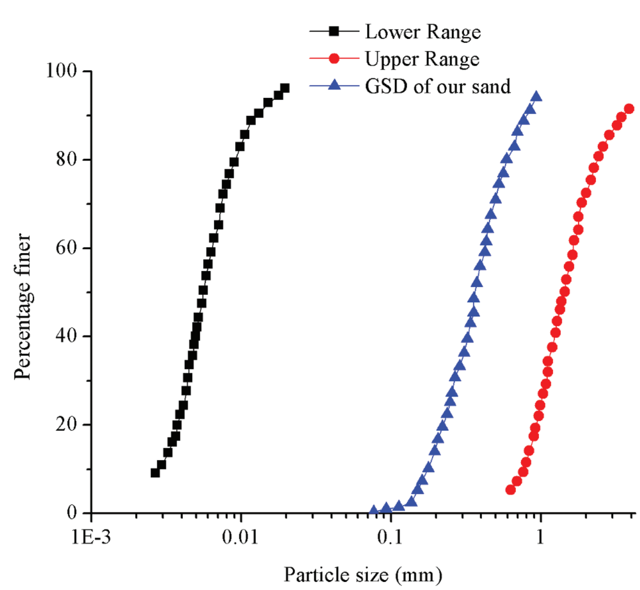

Figure 1. Grain size distribution (GSD) of Kasai River sand along with the liquefaction susceptibility.

proposed by Chattaraj and Sengupta (2016)(as shown in Equation (1)) for Kasai River sand has been utilised for the present numerical study:

$$G_{max} = \frac{611.58 \times Pa^{0.532} \times \sigma^{0.468}}{(0.3 + 0.7e^2)} \quad (1)$$

where 'e' is the void ratio, 'Pa' is the atmospheric pressure, 'σ' is the mean effective stress. Table 1 shows all the material properties for the foundation sand. In addition to the static tests, dynamic tests (such as undrained stress controlled triaxial tests) were performed on this sand for different relative densities (D_R) (40% and 60%) each with CSR values of 0.13, 0.23 and 0.33 with a cyclic frequency of 1 Hz, to find out the liquefaction potential of Kasai River sand. The tests were conducted on cylindrical specimens (70.84 mm in diameter and 120 mm in height) of the sand. As per (ASTM standard D5311 (2011)), height-to-diameter (H/D) ratio of specimen should be within the range of 2–2.5. However, it has been reported in the literature that the ratio in the range of 1.5–3 does not influence the test results significantly (Ravaska (2006)). Thus, the H/D ratio of the prepared specimen for the present study is about 1.6 to remain within the stated range. All the samples are prepared by tamping method as per ASTMD5311–11 guide-lines in three layers with oven dried soil.A funnel with a long tube is used in pouring the soil into the mould.The funnel is raised slowly during the process to maintain zero dropping height of the soil. Depending on the relative density of the sample to be tested, the required amount of sand is calculated for each layer of fill in the mould. After placing the sand into the mould, tamping is applied till it occupies one third height of the mould. The same technique is used to prepare the second and the third layers. Before removing the soil sample from the split mould, a small amount of suction(10–12kPa) is applied to the specimen. Suction makes the samples stiff and consequently disturbance to the sample is reduced while removing the split mould and transferring the soil sample to the triaxial cell. One such test of relative density 60% with a deviator stress (σ_d) of 46 kPa (or CSR ($\frac{\sigma_d}{2\sigma_3}$)value of 0.23) is explained in the paper. The stress-strain loops of this test is plotted in Figure 2(a).A zoomed view of the initial portion of the stress strain loops (Figure 2(b)) shows that there is no strain softening in any of the cycles during the dynamic loading.

Table 1. Material properties for the foundation Kasai River sand.

Parameters for the foundation sand	Value
Mass (saturated) density(kg/m^3)	1994
Cohesion(Pa) (c′)	0
Angle of internal friction, φ′	32°
Poisson's ratio, ν	0.3

If we examine the mode of failure of the sample, it can be said that as the sand is in a medium-dense state with sufficient stress reversal in cyclic loading, the dominant failure mode was referred to herein as limited flow followed by cyclic mobility. The portion of the stress-strain loops in which limited flow occurs is indicated in Figure 2(a,b). It is observed that after cycle no. 6, the sand undergoes dilative behaviour as it touches the phase transformation (PT) line and there is an increase in the shear stress with strain. A further clarification of the dilative nature of sand as well as the onset of limited flow is shown in Figure 2 (c,d).The shear-stress time history along with the excess pore pressure ratio has been plotted for a time span of 6–8 secs in Figure 2(d) in which the entire time history has been divided into loading and unloading portions. It is clearly seen that when there is loading in the soil sample, the excess pore pressure ratio decreases and vice versa, which is a clear indication of the dilative behaviour of the soil.

The liquefaction resistance curve for Kasai River sand is found out from cyclic triaxial tests at 26, 46 and 66 kPa deviator stress for D_R of 40% and 60%. The number of cycles needed for liquefaction in Kasai River sand with the cyclic deviator stress is shown in Figure 3. It shows that the liquefaction resistance of the soil decreases with the increase in the application of deviator stress magnitude and decrease in the relative density.

3. Model calibration of the cyclic triaxial test

Before going for the actual simulation of any experiment, it is again necessary to calibrate the parameters of the constitutive model using the element level tests namely stress-controlled cyclic triaxial test, in our work. A 4-noded plane strain (undrained) quadrilateral element is used to validate the tests. As the tests are load controlled, hence in addition to the initial hydrostatic consolidation effective pressure (100 kPa, in this study) acting on the element as shown in Figure 4(a), a cyclic deviator stress acts on the element with a frequency of 1 Hz (test frequency) till the liquefaction of the soil, as shown in Figure 4(b).

For the validation of these tests, a well-established liquefaction model, namely a bounding surface plasticity model PM4 sand (Boulanger and Ziotopoulou (2015)) is used to study the performance in predicting the results of the element test before going into the simulation of actual shake table test. The PM4 sand model follows the basic framework of the stress-ratio controlled, critical state compatible, bounding surface plasticity model for sand initially presented by Manzari and Dafalias (1997) and later extended by Dafalias and Manzari (2004). This model takes into account the effect

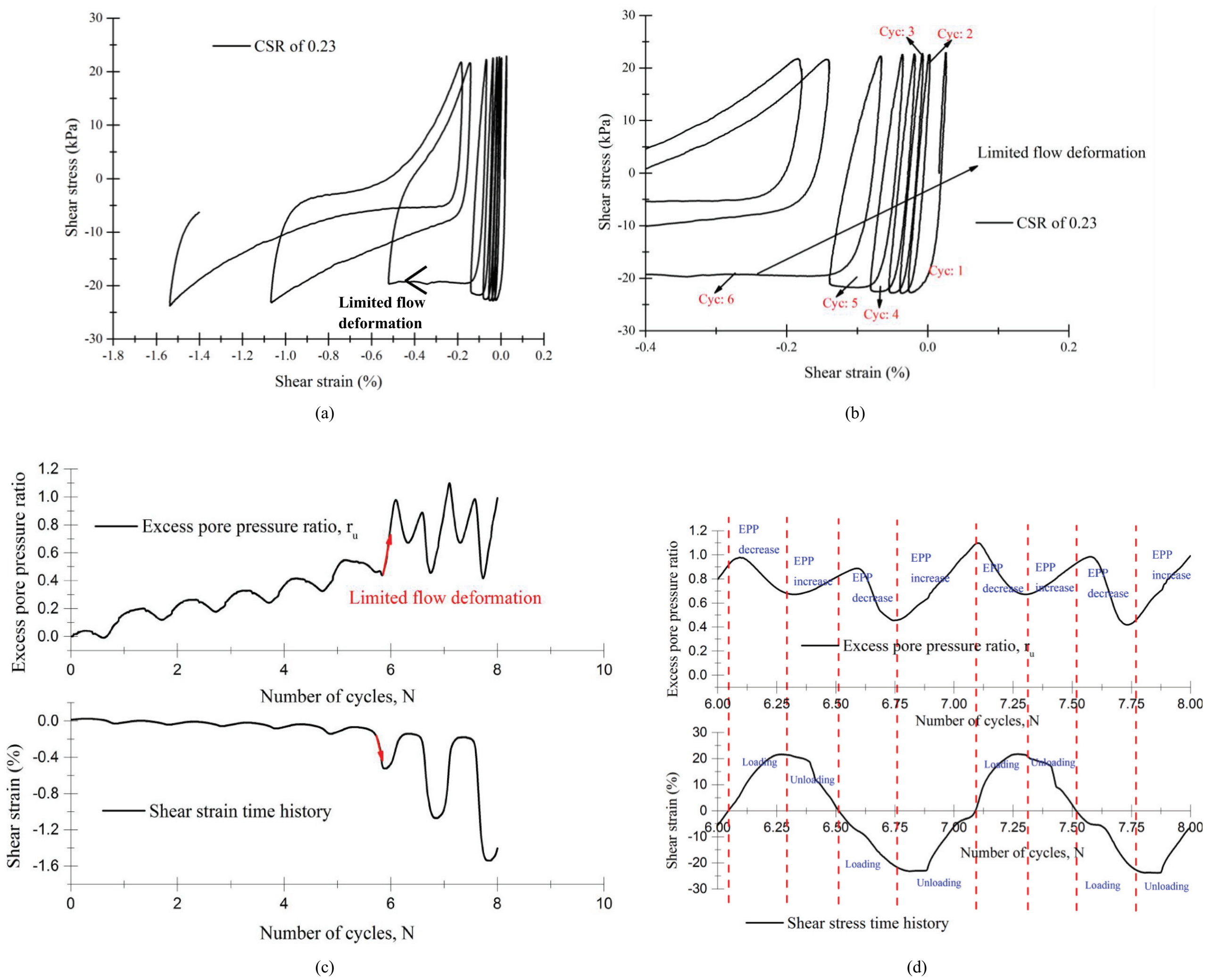

Figure 2. Experimental results of CTX test with 60% D_R for 46 kPa deviator stress.

of fabric changes (in terms of rearrangement of void spaces in the soil, structure and re-arrangement of the soil grains) during dynamic loading by introducing a term known as fabric dilatancy tensor. The fabric-dilatancy related tensor is used to macroscopically model the effect that microscopically-observed changes in sand fabric during plastic dilation have on the contractive response upon reversal of loading direction (Boulanger *et al.* (2011)). The present implementation of the model in FLAC 2D is based on in-plane strains; hence, it limits the usage of this model to plane strain application only. The third out-of-plane direction is considered with an elastic evolution in this model formulation. The PM4 sand model takes into account the elastic and the plastic strain increments which are composed by volumetric and deviator terms.

The elastic strain increments are generated according to acting stress levels and are restricted by the variable shear modulus, G, and the bulk modulus, of the soil material:

$$de^{el} = \frac{ds}{2G}$$

$$de_v^{el} = \frac{dp}{K} \tag{2}$$

The variation of the shear and the bulk moduli (G and K) are given by Equations (2) and (3), using a dimensionless constant (G_0), the Poisson's ratio (ν) and the atmospheric pressure (utilised for normalisation).

$$G_{max} = G_o p_A \left(\frac{p}{p_A}\right)^{1/2} \tag{3}$$

Where, p is the mean effective stress, and the elastic bulk modulus is related to the shear modulus through the Poisson's ratio as,

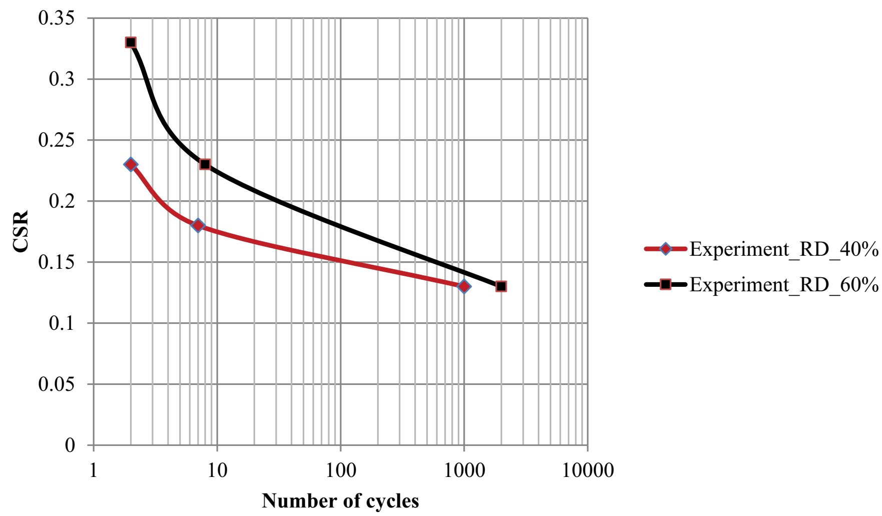

Figure 3. Cyclic stresses needed to produce initial liquefaction.

$$K = \frac{2(1+\vartheta)}{3(1-2\vartheta)}G \tag{4}$$

A value for $G_o$can be estimated on the modified correlation based on the shear wave velocity as:

$$G_o = \frac{\rho(V_{s1})^2}{p_A} / \left(\frac{1+K_o}{2}\right)^{0.5} \tag{5}$$

Where ρ is the dry density of the material, the value of V_{s1} is chosen to match the shear modulus value in line with Equation (1) and K_o is the coefficient of the lateral earth pressure at rest.

The yield surface is defined by Equation (6), representing a cone in a multiaxial space:

$$f = [(s - p\alpha) : (s - p\alpha)]^{1/2} - \sqrt{\frac{1}{2}} pm = 0 \tag{6}$$

where α is the deviatoric back-stress ratio that characterise the yield surface axis and the parameter m controls the size (radius) of the yield surface cone in terms of stress ratio.

This model employs a non-associative flow rule to obtain a realistic evaluation of the plastic strain increments as shown below.

$$d\ \varepsilon_v^{pl} = \langle L \rangle D \tag{7}$$

$$d\ e^{pl} = \langle L \rangle R'$$

Where,L is the loading index, D is the dilatancy, R is the direction of $d\varepsilon_{pl}$, R′is the deviatoric component of R<> are MacCauley brackets that set negative values to zero [i.e. <L ≥ L if L ≥ 0, and <L ≥ 0 if L < 0]. The tensor R is for the assumption of no Lode angle dependency in the π- plane.The dilatancy D relates the incremental plastic volumetric strain to the incremental plastic deviatoric strain by the relation:

$$D = \frac{d\ \varepsilon_v^{pl}}{|d\ e^{pl}|} \tag{8}$$

where, $d\varepsilon_v^{pl}$ is the increment in the plastic volumetric strain, de^{pl} is the increment in the plastic deviator strain. The value of dilatancy (D) is a function of the mean effective stress, deviator stress, initial state of the soil (relative state parameter index, ξ_{cr} = $D_{,Rcs}$-D_R, where $D_{,Rcs}$ is the relative density at the critical state, with respect to D_R-log (p$'$) curve, where D_R is the relative density, p$'$ is the effective stress) and relative density (D_R) of soil (Budhu (2011), Bolton (1986)). For a particular value of D_R of the soil, the dilation angle decreases with the increase in the confining pressure (Budhu (2011)) which can be seen in the pore pressure plot near the surface and near the bottom of the soil. This can be attributed to the crushing of the grains of the soil. When a soil particle tries to roll over another particle, the grain crushes and the crushed particles enter into the existing void spaces, thus reducing the dilation tendency. This phenomenon is incorporated in the model by the framework of the well known stress-dilatancy relationship (Bolton (1986)):

$\varphi_p - \varphi_{cv} = -0.8\psi$ or,

$$\varphi_p - \varphi_{cv} = -0.8\sqrt{\frac{1}{2}}D \tag{9}$$

The state dependency of the dilatancy (D) is modelled as D < 0 (for $\xi > \xi_{cr}$), D > 0 ((for $\xi < \xi_{cr}$) and D = 0 (for $\xi = \xi_{cr}$). Further details about the calculation of the

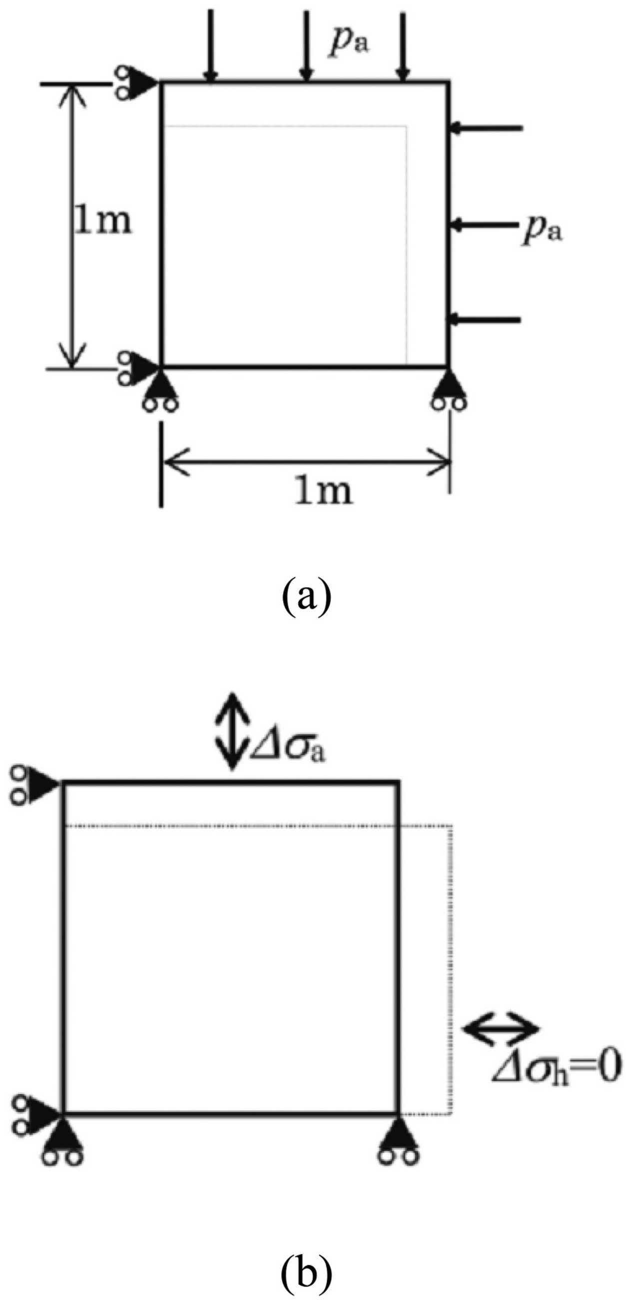

Figure 4. (a) Hydrostatic condition of the soil before the test and (b) application of deviator stress during the cyclic test.

dilatancy parameter (D) involving Equation (9) and the state dependency is elaborated in Boulanger and Ziotopoulou (2015) and not elaborated in this study.

There are three primary input parameters in this model which are to be modified while calibrating with the laboratory tests, and there are several secondary input parameters which can also be obtained during the model calibration. The primary calibrated parameters of the soil model are $N_{1,60}$, C_d and h_{po} The parameters $N_{1,60}$ and C_d are inter-related by the equation (Idriss and Boulanger (2008)):

$$D_R = \sqrt{\frac{N_{160}}{C_d}} \tag{10}$$

Where, D_R is the measure of the actual relative density of the soil. This parameter is very useful as it defines whether the soil will experience contraction or dilation behaviour by means of the relative state parameter index (Bolton (1986)) defined by

$$D_{,Rcs} = \frac{R}{Q - \ln\left(100\frac{p}{p_a}\right)} \tag{11}$$

Where, the value of the secondary input parameters Q and R (critical state parameters) are taken as default values during calibration (Q = 10, R = 1.5), p is the mean effective normal stress. For sands which are loose of critical states, the value of $\xi_{cr}>0$ and $D_{,Rcs}< D_R$ and vice versa. The primary variable that adjusts plastic volumetric strains during contraction is h_{po} (contraction rate parameter), whose value is found to be 0.47. This value is adjusted based on the volumetric strain and the shear strain responses of the soil. The model uses bounding, dilatancy and critical surfaces according to Dafalias and Manzari (2004). The current version of the model has been simplified by removing the Lode angle dependence. So the friction angles are the same for compression or extension loadings. The bounding and the dilatancy ratios are related to the critical stress ratio, M by the following equations:

$$M_b = M\ \exp(-n_b\xi_{cr})$$

$$M_d = M\ \exp(n_d\xi_{cr})$$

$$M = 2\sin\left(\varphi_{cv}\right) \tag{12}$$

Where, the model parameters $n_b$and n_d define the computation of $M_b$and M_d with respect to M. The bounding stress ratio controls the relationship between the peak friction angle and the relative state. During shearing, the bounding and the dilatancy surfaces approach the critical surface at the same time the relative state parameter index approaches the critical state line (R tends to zero). The bounding surface framework aims to simulate the plastic deformations within the yield surface. The dilatancy surface defines the location where transformation from contractive to dilative behaviour occurs, also known as transformation phase state (PT).

The initial location of the bounding surface (M_b), dilatancy surface (M_d) and the critical state surface (M) for the state of a sand in the 'loose or dense of critical' is $M_d \geq M > M_b$ and $M_b > M > M_d$, respectively. When the sand is loose of critical, the critical state angle and the dilatancy angle are relatively close to each other. Under undrained cyclic loading, the change in the effective stress is associated with the shear-induced volumetric dilative or contractive tendency of the soil.

It is to be noted that the yield surface is an open-ended cone in Equation (6) (there is no cap at the end). Due to which there is no plastic volumetric strain under constant stress ratio loading (only elastic volumetric strain is admissible as per Equation (2), as the stress path is inside the cone and moving along a line parallel to the outer surface of the cone). Hence, the model is modified to account for the post-liquefaction volumetric strain (occurs at constant stress ratio) by reducing the post-shaking elastic shear modulus G (and hence elastic bulk modulus K) which increases reconsolidation strains, thereby compensating for the volumetric strains which are not explicitly modelled. In this paper, we are interested in the overall behaviour of a piled raft which occurs during a dynamic excitation (which occurs at variable stress ratio); hence, we need not have to worry for the case of constant stress ratio loading.

The value of constant volume friction angle, φ_{cv} is taken as 34° and the value of n_b (controls the rate at which the bounding surface approaches the critical surface) is taken as 0.4. The values of the calibrated input parameters are tabulated in Table 2. The experimental and the numerical (PM4 sand) stress–strain curves, pore pressure time histories and the effective stress paths for CSR values of 0.23 (D_R 60%) (Figure 5(a,c)), 0.18 (D_R = 40%) (Figure 6(a-c)) and 0.23 (D_R = 40%) (Figure 7(a-c)) are shown. It is to be noted that as the simulations are conducted in plane strain compression, hence the asymmetric nature of the stress-strain loops are not properly captured as observed in the experiment. It is seen that there is a good match between the prediction and the experiments along the effective stress paths of the test, although in Figures 5(c),6(c) and 7(c), the experiment has a tendency to incline towards the left and then proceed towards liquefaction, which is not captured by the model.

After this numerical study, we are interested in the numerical prediction of the cyclic resistance curves obtained from the experiments for D_R of 60 and 40% using the model parameters given in Table 2. In order to find out the curves, the element of size 1 m x 1 m is subjected to various values of CSR values till the soil liquefies. The CSR values versus number of cycles to liquefaction for DR of 60 and 40% is plotted in Figure 8. The overall match is quite good upto 100 cycles which is the extent of our area of interest. For the completion purpose, one experimental point has been added for 1000 cycles. From these observations, we find that it is quite appropriate to go further with PM4 sand model for the validation of the shake table tests.

Table 2. Calibrated parameters of PM4 sand for Kasai River sand.

Parameters of PM4 model	Values
$N_{1,60}$	9 (for D_R 40%), 15 (for D_R 60%)
V_{s1} (based on the relationship derived by Chattaraj and Sengupta (2016))	221 (for D_R 40%), 228 (for D_R 60%)
h_{po}(controls the rate of contraction)	0.47
φ_{cv}(constant volume friction angle)	34
n_b(controls the bounding ratio)	0.4
h_o	0.2
Q (Critical state line (CSL) parameters)	10
R (Critical state line (CSL) parameters)	1.5

4. Experiment of piled raft on saturated sand

The liquefaction tests on the sand are carried out on the uniaxial shake table in 1-g (actual gravity loading) environment within a transparent Perspex container of size 1000 mm x 825 mm x 858 mm. In a liquefaction test, the sample preparation is a major issue because the density and the water content of the sand should be maintained uniform throughout the sample. Mullins *et al.* (1977) have given a description of the effect of sample preparation on sand liquefaction and concluded that the liquefaction response of a soil specimen significantly depends on the method of sample preparation. A 650-mm thick sand bed is prepared inside the test chamber with D_R of 43%. A pre-calculated amount of water is added to fully saturate the sand (30.56%) within the test chamber. All the liquefaction tests are conducted with water table at the top surface of the sand bed. In this model test, a single piled raft is placed on the top of the sand surface at the middle of the test tank. The present experiment follows the 1-g scaling law proposed by Iai (1989) and Wood (2004). The scale factor (λ) utilised in the model study to scale down the different parameters is 20. It is to be noted that the small strain modulus of soil depends on the square root of the applied stress ($E \propto \sigma^{0.468\ (\sim 0.5)}$ as in Equation (1)), and as the stress (σ) is scaled by λ, hence the strain (ε) needs to be scaled by $\lambda^{0.5}$ (instead of 1.0, which is commonly used). Table 3 displays the 1-g scaling relationships utilised in this study.

The dimensions of the soil bed inside the test tank are 1 m (L) x 0.825 m (B) x 0.65 m (H). This is corresponding to a prototype dimension of 20 m (L) x 16.5 m (B) x 13 m (H). The relative density of the saturated sand used in the model test is 43%. In order to *'replicate the same behaviour (contraction and dilation) of the sand from model to prototype'* for the saturated sand, it is necessary to keep the relative state parameter index (ξ_{cr}) of the soil constant in both the model and the prototype (Roscoe and Poorooshasb (1963)). If the initial state of the soil element (in the model and the prototype) on an e-ln(σ')

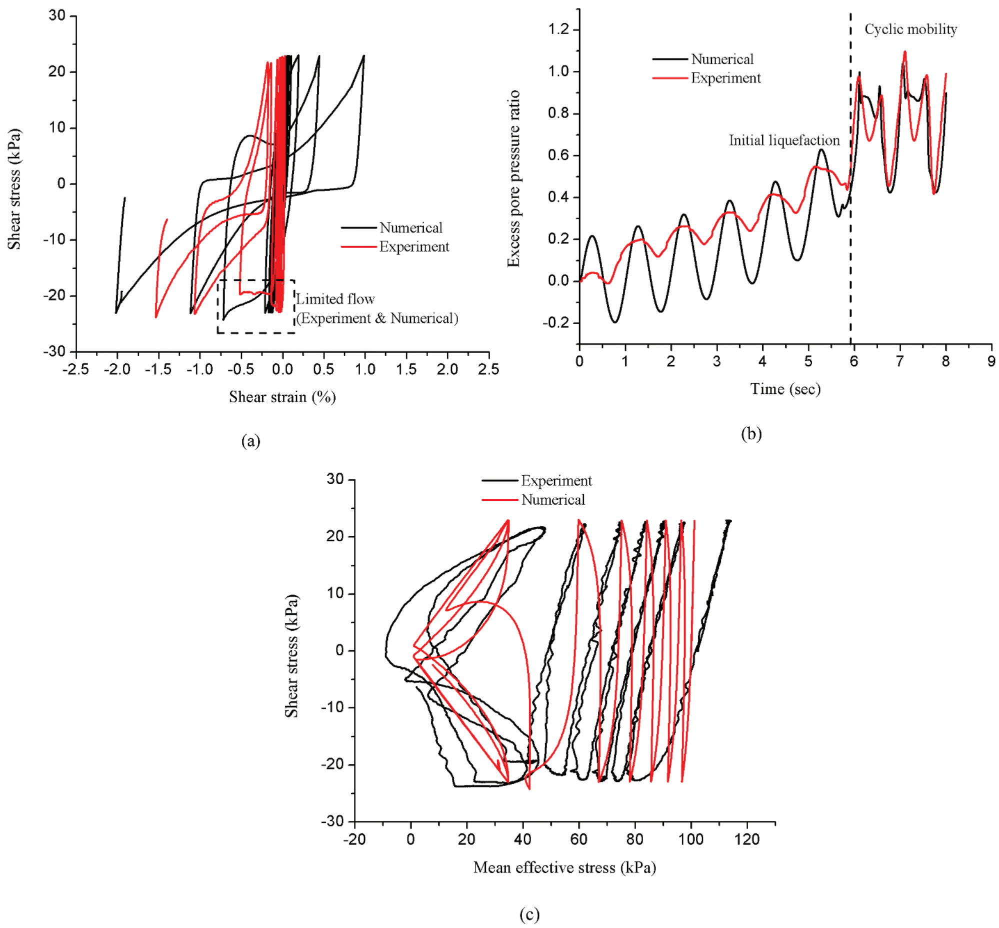

Figure 5. Comparison of experimental and numerical results: (a) Stress-strain curve, (b) Pore water pressure time history and (c) Effective stress path for D_R of 60% with CSR 0.23.

plot are equidistant from the critical state line (CSL), then the stress paths will be geometrically identical as shown in Figure 9(a). This figure shows the projection of the critical state curve on τ-σ' plane showing geometrically similar stress paths for the model (A_m) and the prototype (A_p). For Kasai River sand, the value of Q = 10 (for Quartz sand) and R = 1.5 have been assumed (Bolton (1986); Boulanger and Ziotopoulou (2015)) in this study (refer to Table 2 and Equation (11)). The value of the relative state parameter index (ξ_{cr}) in the shake table test is −0.25556 (0.174443–0.43) (for the mean confining stress of 4.06 kPa) and this is maintained in the prototype also (for the mean confining pressure p of 89.69 kPa). Thus the relative density of the prototype soil is 52.81% as illustrated in Figure 9(b).

A 6 m x 6 m prototype square concrete (M20 grade) raft foundation of 430 mm thickness (by scaling the footing flexural rigidity with the stiffness of the soil (Wood (2004))) has been modelled by a square raft foundation of dimensions 300 mm x 300 mm x 15 mm (length, breadth and thickness) with M10 grade of concrete. A prototype pile of 9 m in length and 667 mm in diameter (by scaling the pile flexural rigidity with the stiffness of the soil (Wood (2004)))of M 20 grade of concrete underneath the raft is modelled by a single circular M 10 concrete pile of 25 mm in diameter and 450 mm long. The pile is located at the centre of the raft. In the model raft, a square steel wire mesh (chicken mesh) with 3 mm square openings has been used as the reinforcement. The steel wires are of 1 mm in diameter. The reinforcement cages of the piles are prepared using the same steel wire mesh with 3 mm openings. The pile reinforcements are attached to the reinforcement of the raft maintaining a 50 mm lap length in all directions. Figure 10 shows the reinforcement details for the case of a piled raft with a single pile. The pile along with the raft is casted monolithically using M10 grade concrete. A nominal mix of 1:3:6 of ordinary Portland cement, fine sand and coarse aggregates is utilised for the purpose. The coarse aggregate size is so chosen that the mix can pass through the steel reinforcement mesh of the raft and the pile. After the casting, the models are soaked in

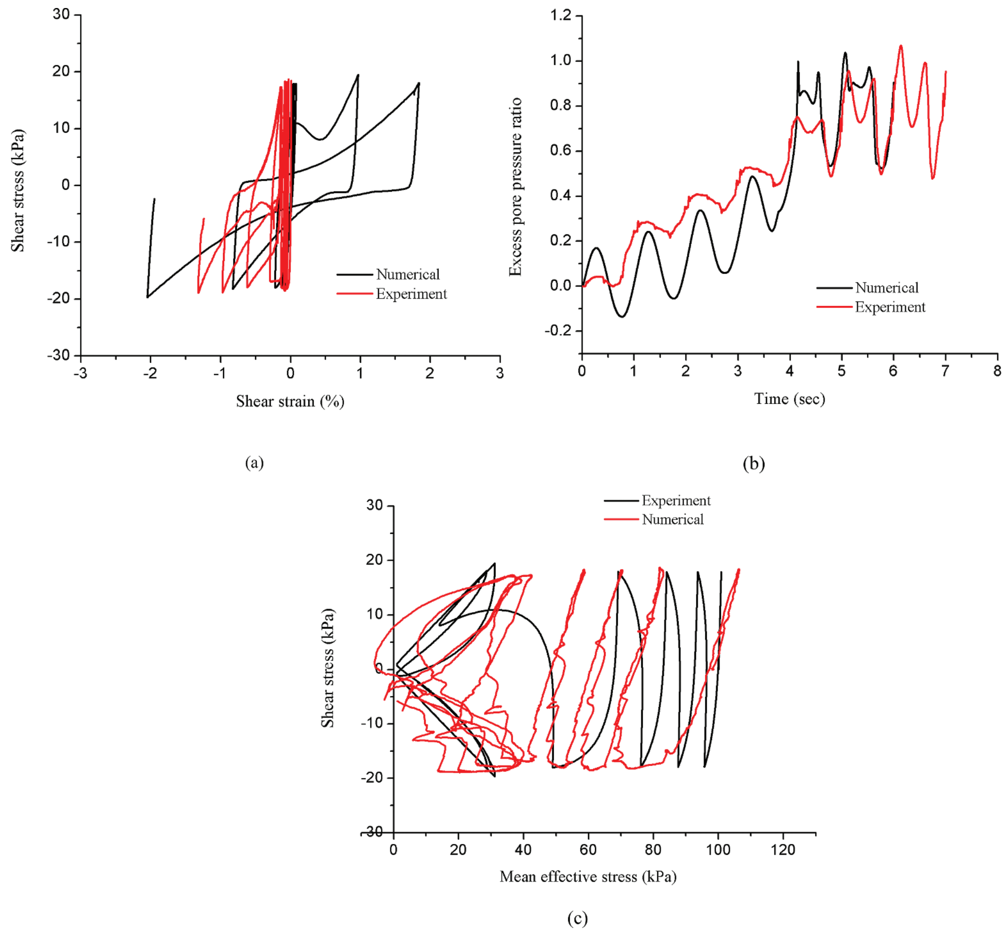

Figure 6. Comparison of experimental and numerical results: (a) Stress-strain curve, (b) Pore water pressure time history and (c) Effective stress path for D_R of 40% with CSR 0.18.

water and allowed to cure for more than 28 days. A vertical surcharge pressure of 1.445 kPa (13 kg) is applied on top of the model raft. The above surcharge pressure is equivalent to a 28.9 kPa surcharge pressure in the prototype scale and represents the vertical load of a single bay, three storied building (using 1-g scaling law, Iai (1989)). A 32 mm thick thermocol sheet is placed on three sides of the test chamber to minimise the reflection/refraction of P-waves from the boundaries (Banerjee *et al.* (2017)). Accelerometers are placed at the top and the bottom of the sand in the test chamber. In addition to the accelerometers, three pore water pressure transducers at the middle location of the test chamber and at 11.5 cm, 31 cm and 52 cm from the top surface of sand are utilised to monitor the pore water pressure development in the sand bed during the shaking. The test setup is shown in Figure 11.

The static water level in the sand bed within the test tank is measured before the commencement of the dynamic tests. The pore water pressure at each pore pressure sensor location is recorded to determine the initial static piezometric height. The pore water pressure fluctuations at the specified locations are measured during the shaking test and the liquefaction of the sand is assessed. The soil is considered liquefied when the ratio of the pore water pressure to the initial total stress within the soil is close to one. Figure 12 shows the variation of the pore water pressure with time at various depths within the sand bed during the laboratory model test.It may be noticed that the pore water pressure at the mid depth of the sand dissipates faster than that at the bottom of the sand bed. This is attributed to the length of the drainage path that the excess pore pressure tries to find after the shaking stops.

5. Input motions

For the liquefaction study, a number of earthquake motions are reviewed and 09/03/2010 Darfield, Christchurch Earthquake ($M_w = 7 \cdot 1$, S73W component) motion is selected (conservatively). The maximum acceleration, *a*, maximum velocity, *v*, maximum displacement, *d*, and predominant period are 490.5 cm/s^2, 26.77 cm/s,

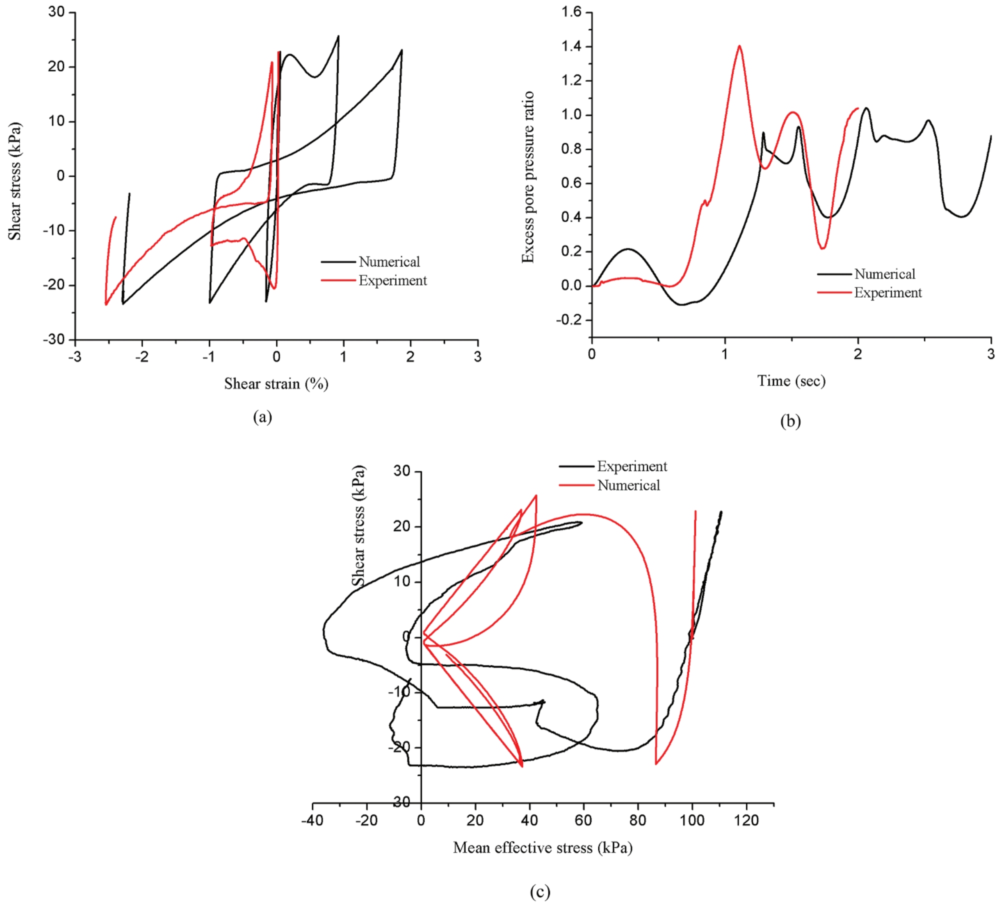

Figure 7. Comparison of experimental and numerical results: (a) Stress-strain curve, (b) Pore water pressure time history and (c) Effective stress path for D_R of 40% with CSR 0.23.

10.58 cm, and 0.4s (2.5 Hz), respectively, for the selected motion. As before, following the procedure developed by Seed *et al.* (1975) to convert an actual irregular stress time history into repetitive stress cycles of constant amplitude, the equivalent acceleration time history is constructed. The $M_w = 7.1$ Earthquake is modelled by 10 cycles of identical full sinusoidal waves of average amplitude, a_{avg} of $0 \cdot 35$ g at a frequency of 2 Hz. The corresponding displacement time history is applied at the base of the shake table at a time step of 0.01953sec, as shown in Figure 13.

Figure 14 shows the readings of the accelerometers located at the top and the bottom of the sand foundation. It is to be noted that the top accelerometer shows unsymmetrical response which occurs due to the lateral motion of pile raft inside the soil. The bottom accelerometer is far away from the influence of pile raft, hence the bottom accelerometer shows symmetrical response. The PGA amplification through the 0.65 m of Kasai River sand is found out from the ratio of the measured maximum (absolute) value of accelerations from the top and the bottom time history. The amplification of the motions (with time step = 0.01953 sec.) through the sand is found to be 2.2 times for the saturated sand in the experiment.A similar observation for amplification in the acceleration for the liquefiable deposits has been observed by Wang *et al.* (2019), Zeghal and Elgamal (1994). This is contrary to the expectation of a reduction in the acceleration through a soil during liquefaction. The small-scale laboratory studies by Wang *et al.* (2019) on pile group supported bridges have shown that the physical mechanism that produces such phenomena is the dilatant nature (cyclic mobility) of cohesionless soils, which introduces the partial recovery of the shear strength under cyclic loading. This recovery translates into the ability to produce large deformations (because the rollover of each particle over another requires greater deformation than the slip down phenomenon of each particle) which follows large and spiky acceleration records. This phenomenon is site related, not source related.

6. Numerical simulation of piled raft on saturated Kasai River sand

Before the actual simulation, the nature of the strain-dependant stiffness and the damping ratio of the soil need

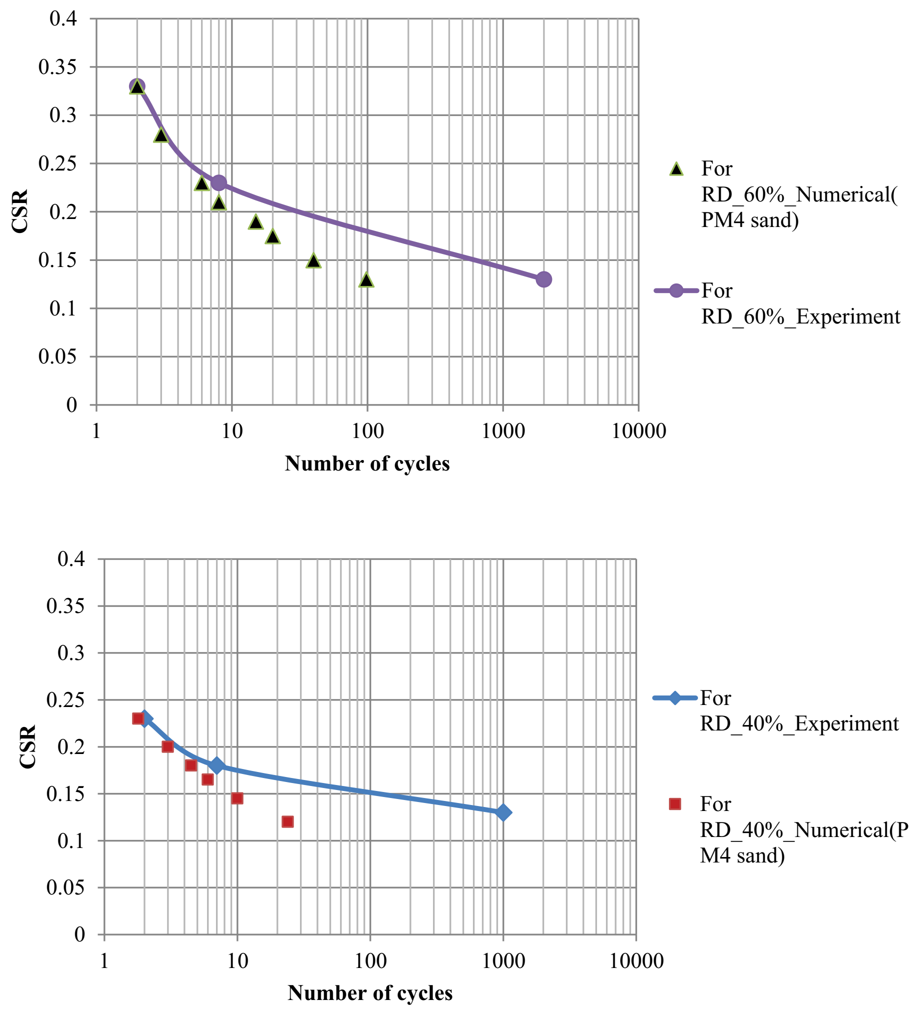

Figure 8. Comparison of experimental and numerical cyclic resistance curves for D_R 60% and 40%, respectively.

Table 3. 1-g scaling law (λ = 20 (=prototype/model)).

System variables	Geometric scaling factor
Mass density	1.0
Acceleration	1.0
Velocity	$\lambda^{0.75}$
Displacement	$\lambda^{1.50}$
Length	λ
Stress	λ
Time	$\lambda^{0.75}$
Strain	$\lambda^{0.5}$
Frequency	$\lambda^{-0.75}$
Pore pressure	λ

to be checked. For this purpose, the experimental G/G_{max} and the damping ratio curves at the effective confining stress of 100 kPa (D_R = 40%) are compared numerically using the calibrated soil parameters given in Table 2. For the comparison of G/G_0 curve ($G_0 = G_{max}$ = maximum shear modulus), a single finite element (under undrained condition) is subjected to a gradually increasing strain from 0.0001% to 10% with each strain amplitude continuing up to 3 cycles. The element is subjected to a mean effective confining stress of 100 kPa in all directions and the stress-strain loops are obtained. Figure 15 shows a comparison between the laboratory test data and the model predictions for Kasai River sand.

It is to be noted that the cyclic tests are performed at an effective confining stress of 100 kPa, whereas the soil in the shake table is at a mean confining pressure of 4.06 kPa. For this, the G/G_{max} curves need to be validated for 4.06 kPa. As the cyclic triaxial and the resonant column tests are not performed at this stress, hence the theoretical G/G_{max}curves proposed by Menq (2003) are fitted with the experimentally obtained values of G/G_{max} for 100 kPa. The analytical expression for the estimation of the cyclic strength degradation of a sand as proposed by Menq (2003) is given by:

$$\frac{G}{G_o} = \frac{1}{(1+\frac{\gamma}{\gamma_{ref}})^a} \tag{13}$$

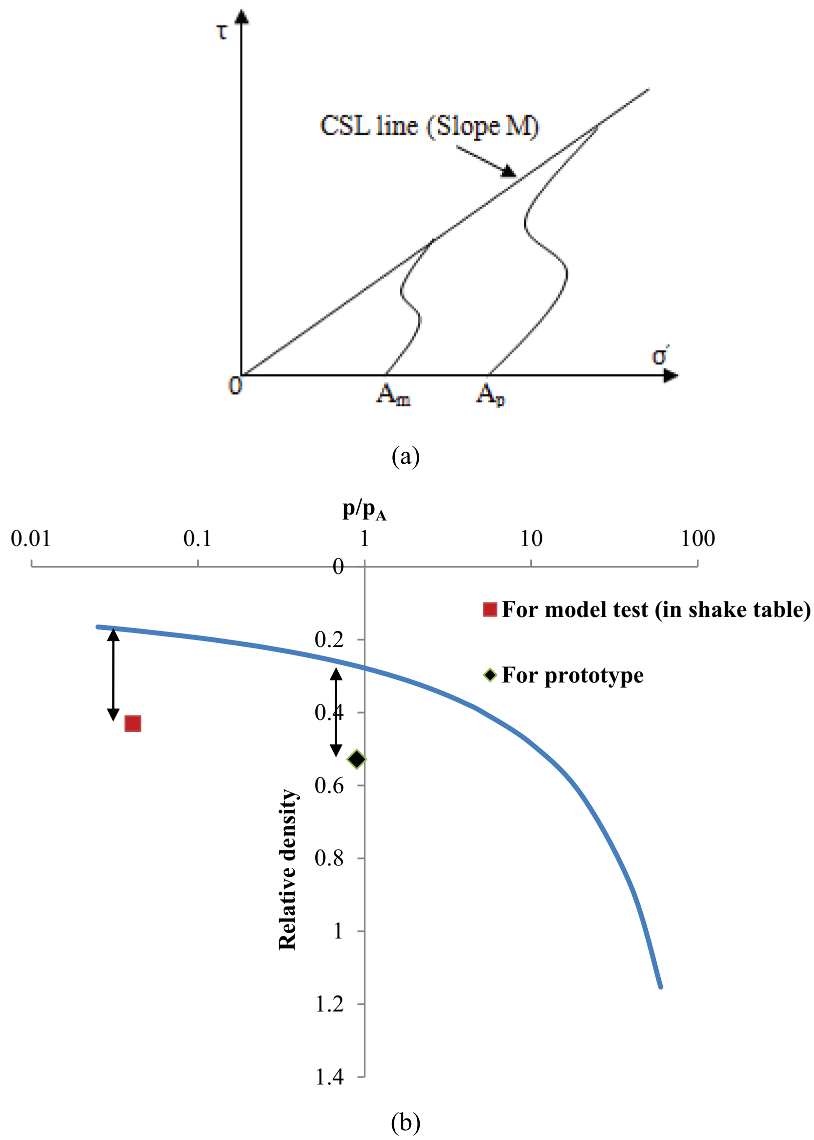

Figure 9. (a) A schematic diagram of geometrically similar stress paths and (b) the location of relative state parameter index for the model and the prototype soil.

and

$$\gamma_{ref} = A_{\gamma}\left(\frac{\sigma'_m}{P_a}\right)^{n_{\gamma}} \text{and}\, a = 1.24 + 0.1\log\left(\frac{\sigma'_m}{P_a}\right) \quad (14)$$

The constant parameter, A_{γ} is estimated as $0.07C_u^{-0.5}$. Where, C_u is the coefficient of uniformity (=2.84, in this study) and the exponent, n_{γ} is estimated as $0.5C_u^{-0.15}$for Kasai River sand. The above equations are utilised for estimating the modulus degradation curve for Kasai River sand at a confining pressure of 4.06 kPa. After the estimation, the values are compared numerically in Figure 16, using the same calibrated parameters as reported in Table 2.

It is observed that the model performance is good throughout the strain range, hence the parameters in Table 2 for predicting the responses of the shake table tests are valid. The two-dimensional finite difference analyses of a 0.65 m of Kasai River sand bed, as tested on the laboratory shake table, are performed using a commercial software called FLAC2D (Itasca (2005)). The 300 mm x 300 mm x 15 mm square concrete raft foundation is numerically discretized by six numbers of two-dimensional beam elements. A beam element has three degrees of freedom (two displacements and one rotation) at each node. The beam elements are assumed to be elastic. The pile is modelled using pile elements in FLAC 2D (Itasca (2005)). The pile and the raft are modelled as elastic materials with modulus of elasticity (E) of 1.58×10^{10} Pa (using the formulation, $E = 5000\sqrt{f_{ck}}$ (in MPa) as recommended in IS 456 (2000)

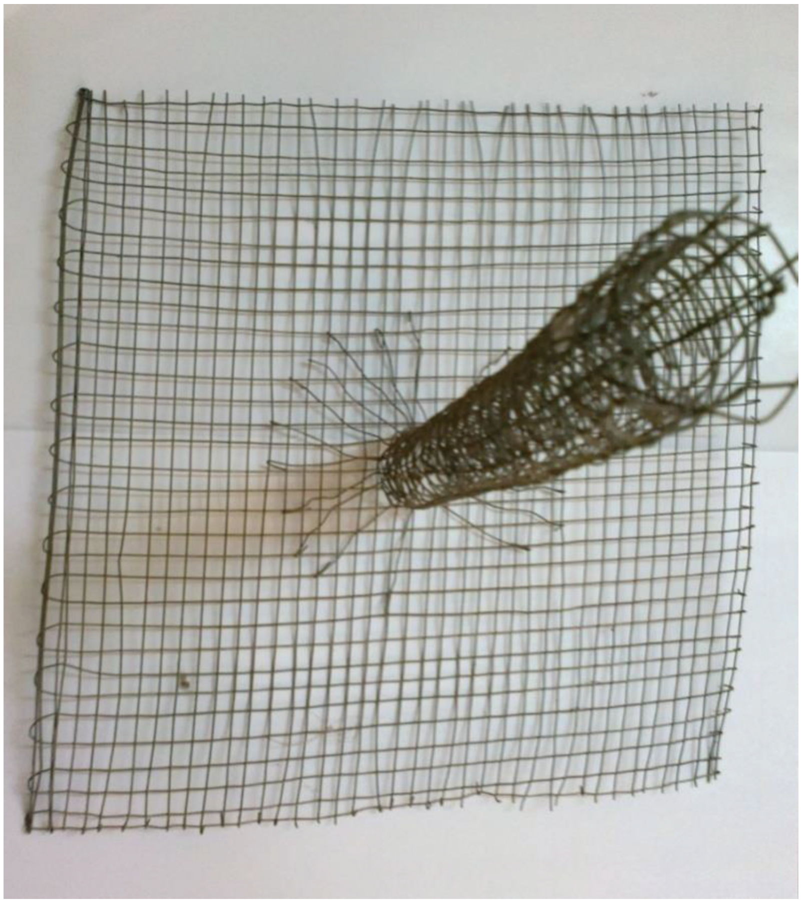

Figure 10. Reinforcement details of the piled raft model.

with Poisson's ratio of 0.15, length of 450 mm and diameter of 25 mm. The locations of the side and the bottom boundaries in the numerical analyses are chosen to satisfy the dimensions of the sand bed in the shake table model tests. The foundation sand bed (1.0 m in width and 0.65 m in height), is discretized by 31 × 7 numbers of quadrilateral elements, each of size 0.092 m × 0.0322 m as shown in Figure 17. The

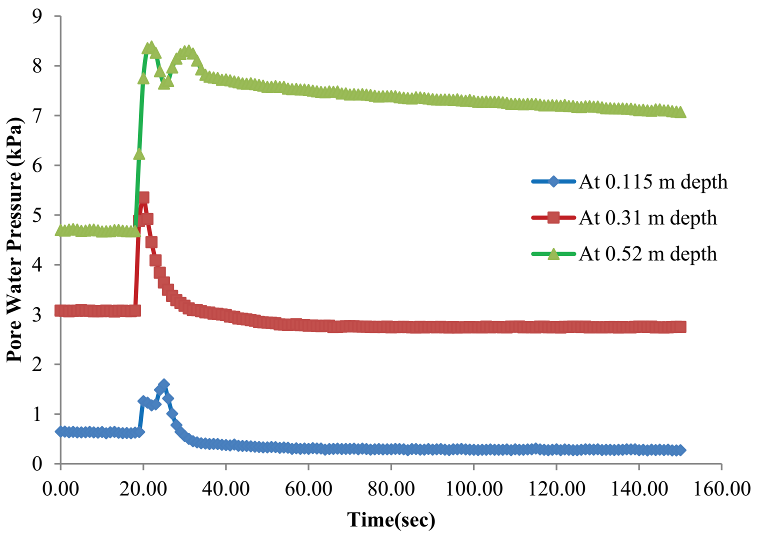

Figure 11. A view of the test setup and the locations of the accelerometers and the pore water pressure transducers.

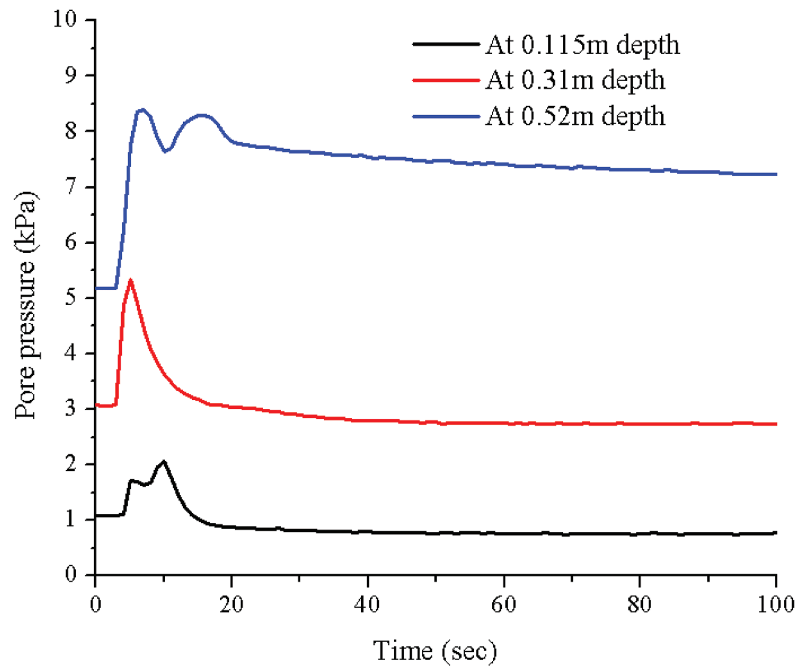

Figure 12. Variation of pore water pressures within the sand bed with time.

Plexiglass test chamber, within which the laboratory model tests are conducted, is not modelled in the numerical analyses. In the static analysis, the soil-structure system is under gravity loading. The soil model adopted is PM4 sand during the static analysis. The bottom boundary is fixed in all the directions and the side boundaries are fixed in the horizontal (x) direction only as shown in Figure 17. The static/seismic behaviour of the piles is a three dimensional problem. The pile formulation simulates a row of equally spaced piles in plane-strain. In FLAC 2D (Itasca (2005)), a linear scaling of the material properties of piles is internally done as per out-of-plane spacing. The out-of-plane spacing has been taken to be 1 m, such that the ratio L/D = 40,

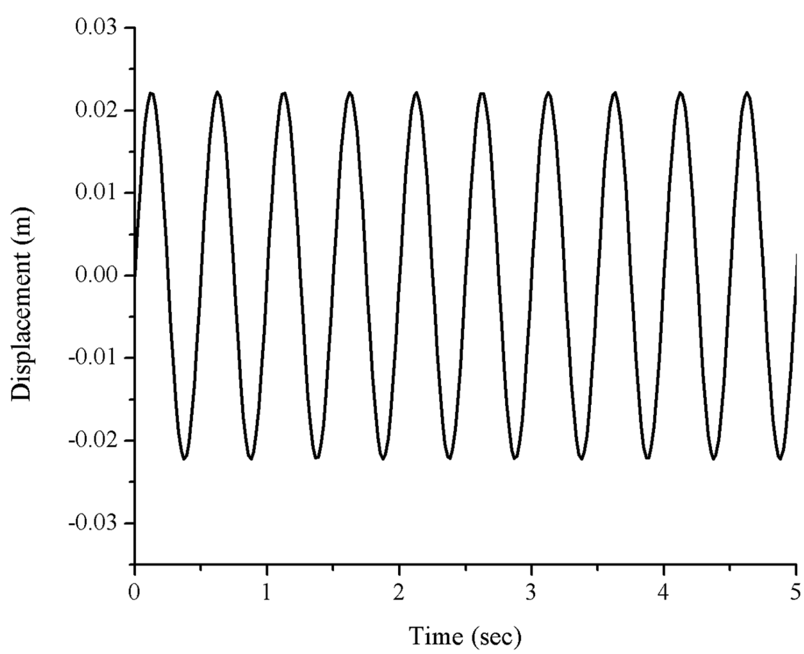

Figure 13. Displacement time history for the liquefaction study.

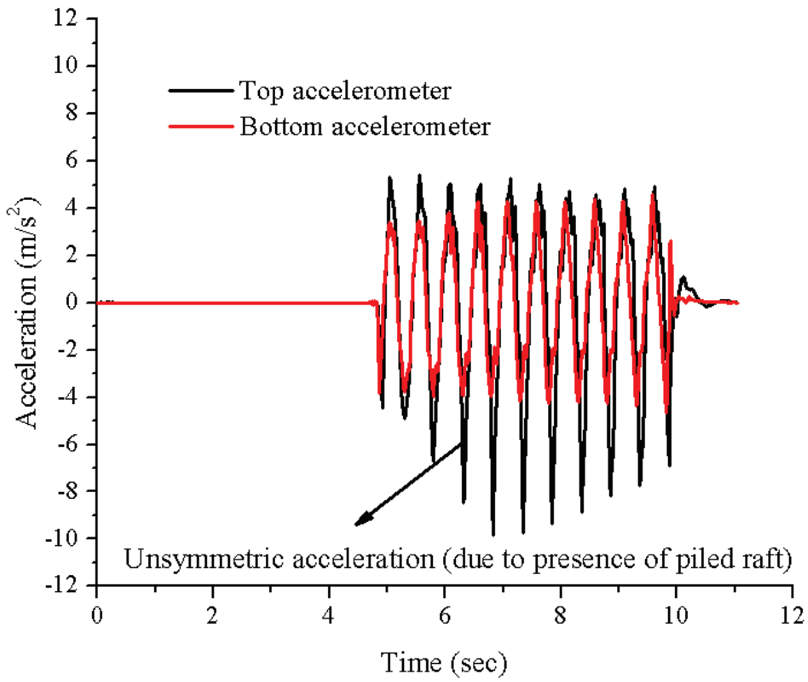

Figure 14. Accelerometer readings at the top and the bottom of the foundation sand with piled raft.

where L is the c/c distance between the piles (=1000 mm) and D is the diameter of the pile (25 mm). This ratio must be greater than 5, so that the piles no longer influence each other and the soil starts to flow between the piles. After performing the initial static analysis, the dynamic analysis is performed. In the dynamic modelling, the wave propagation through the soil (media) is of considerable importance. The finite difference grid dimensions are selected by considering the maximum frequency (*f*) of the shear wave that the model could logically respond to during the dynamic loadings (=20 Hz). In any highly nonlinear simulation, the shear modulus/shear wave velocity reduces drastically. The element size used in this study is given by:

$$\Delta l = \frac{Vs, \min}{10f} \tag{15}$$

where, $V_{s,\min}$ is the minimum shear wave velocity of the sand and Δl is the element size in the numerical model. For the dynamic analyses, tie boundaries are adopted, in which the opposite nodes are connected by master-slave for both degrees of freedom. This is due to the limitation of PM4 sand model which is not developed for the free field boundaries. The value of the pore water pressure is fixed at the top surface of the soil throughout the dynamic analysis. The same acceleration-time history (in terms of velocity), applied to the shake table in the laboratory model tests, is assumed to be acting at the bottom of the soil domain in the numerical analysis. The magnitude of the maximum acceleration is 3.505 m/s^2 (0.3505 g). The soil behaviour under the dynamic loading is described by the bounding surface plasticity model PM4 sand whose parameters are already shown in Table 2. The interaction between the raft/pile and the foundation soil is modelled using a shear and a normal spring at each of the common nodes between the raft and the soil. The interface parameters, suchas normal and shear stiffness ($k_n$and k_s) are estimated from the bulk modulus (K) and the shear modulus (G) of the foundation soil using the relationship (Itasca (2005)):

$$k_n = k_s = 10\frac{\left(K + \frac{4}{3}G\right)}{\Delta z_{min}} \tag{16}$$

Where, *K* and *G* are the bulk and the shear moduli of the soil at a depth where the structure is located. Δz_{min} is the smallest width of an adjoining element in the respective normal direction. The frictional resistance of the shear coupling spring is assumed to be equal to 2/3rd of the internal friction of the soil (=23°) and a small amount of cohesion (10 kPa) is assumed in both normal and shear directions (Itasca (2005)).As the model has a small 'purely' elastic region with the size of the yield cone governed by a parameter 'm' (Equation (6)), hence any stress reversal within the yield cone (Equation (6)) will lead to a purely elastic response (i.e. the loading and unloading paths will be same) and there will be no energy dissipation. Hence, the model underestimates the damping ratio at small strains.

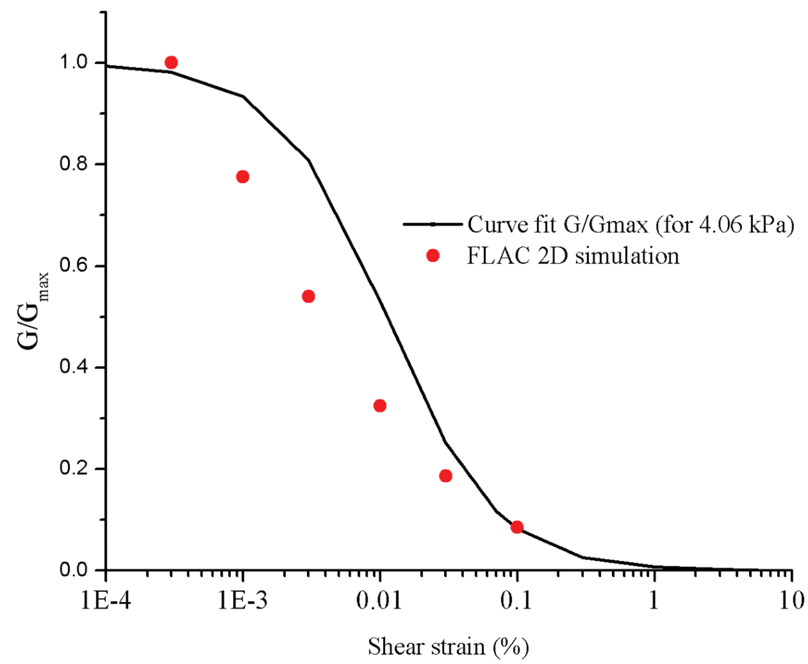

Figure 15. Comparison between the curve fitted data and the model predictions for Kasai River sand at an effective confining stress of 4.06 kPa.

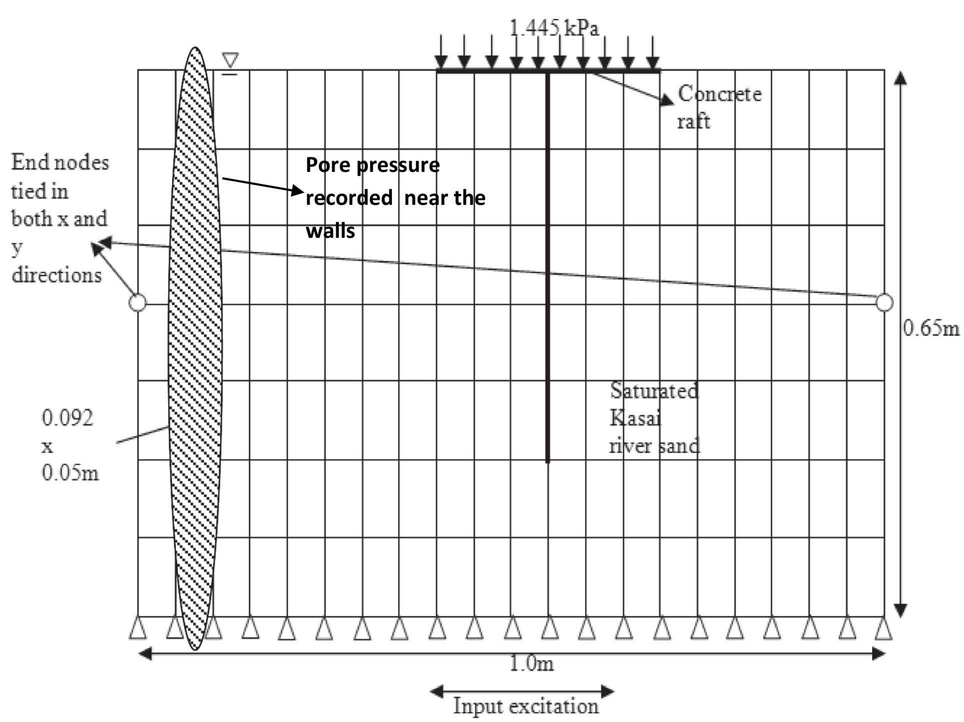

Figure 16. Comparison between the laboratory test data and the model predictions for Kasai River sand at an effective confining stress of 100 kPa.

To account for this problem and to suppress the high-frequency noise in the response time histories, a small value of1.5% Rayleigh damping has been added in addition to the hysteretic damping of the soil with a frequency of 12 Hz.The entire analysis is performed with 'flow off' and no dissipation of the excess pore water pressure is allowed after the motion has ended. The vertical deformations of the foundation soil at the end of the static and the dynamic loadings are shown in Figure 18(a,b). It is observed that the soil (or piled raft) has undergone a vertical settlement of

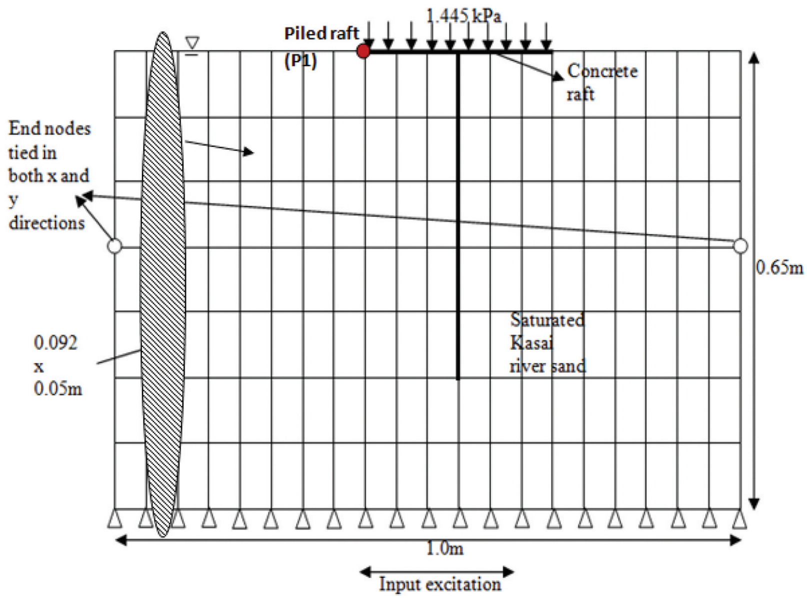

Figure 17. Schematic diagram of the numerical model.

0.75 mm at the end of dynamic excitation. The experimentally obtained acceleration time history, in both time and frequency domains, at the top of the sand foundation is compared with that obtained from the numerical study and shown in Figure 19.

It is to be noted that the Fourier amplitude depends on the number of points and the time step in the time history recordings. The amplitude does not match because the number of points and time step in the numerical analysis are 8549 and 0.000581 secs, whereas in the model test, they are 309 and 0.01953 secs. While comparing, we are interested in the frequency contents rather than the amplitudes which may or may not match. The numerical results match reasonably well with the results obtained from the shake table test. From Figure 19(b), it may be noted that the odd harmonics of the input motion are very much predominant numerically and the peaks match with the experimental results (only odd ones) quite well. But there are some peaks which are still unexplained in the experiment. The numerical stress–strain curve found near the centre of the soil located 3.5 m below the piled raft foundation are shown in Figure 20, in which the dilation peaks or the strain hardening portions which are identified to be the cause of the amplification of the acceleration through the soil are clearly seen. In Figure 19(b), the generation of the odd harmonics of the input motion in the response acceleration is a by-product of the sharp corners in the stress-strain loops (Figure 20) as explained by Veeraraghavan *et al.* (2019). The variation in the excess pore water pressure, U_{excess} in the sand with time at 0.115 m, 0.31 m and 0.52 m depths below the piled raft foundation is recorded during the test and validated numerically as shown in Figure 21(a-c). From Figure 21(a-c),it may be observed that the pore water pressures are close to the total vertical stress and it can be said conclusively that the soil has liquefied at a depth of 0.31 m and 0.52 m, numerically. As the experimental pore water pressures are recorded at 1 sec interval, hence itis very difficult to say that the soil has not liquefied experimentally. From the numerical analysis of pore water pressure histories, the time instant of drops in the pore water pressure is related to the spike in the acceleration records. When the pore water pressure drops, the stress-strain curve has a strain hardening characteristic due to which the stiffness of the soil increases resulting in a sharp amplification in the response accelerations. Also, it is observed that due to extensive contraction and dilation of soil particles, the pore water pressure oscillates with a frequency twice that of the input motion.As the soil is tested at a relatively low confining pressure and at a large input displacement, the combined effect of both of these factors lead to an extensive dilation of the soil due to which the response acceleration gets amplified. A similar phenomena has been reported by Wang *et al.* (2019), Dash and Bhattacharya (2015) in the shake table and the centrifuge studies of pile supported foundations. The numerical predictions match quite well with the experimental observations and thus validates the numerical study.

6.1. Effect of amplitude of input motion on the responses of model piled raft

The effect of the amplitude of input motion on the seismic responses of a piled raft is investigated by applying harmonic acceleration with PGA of 0.35 g at

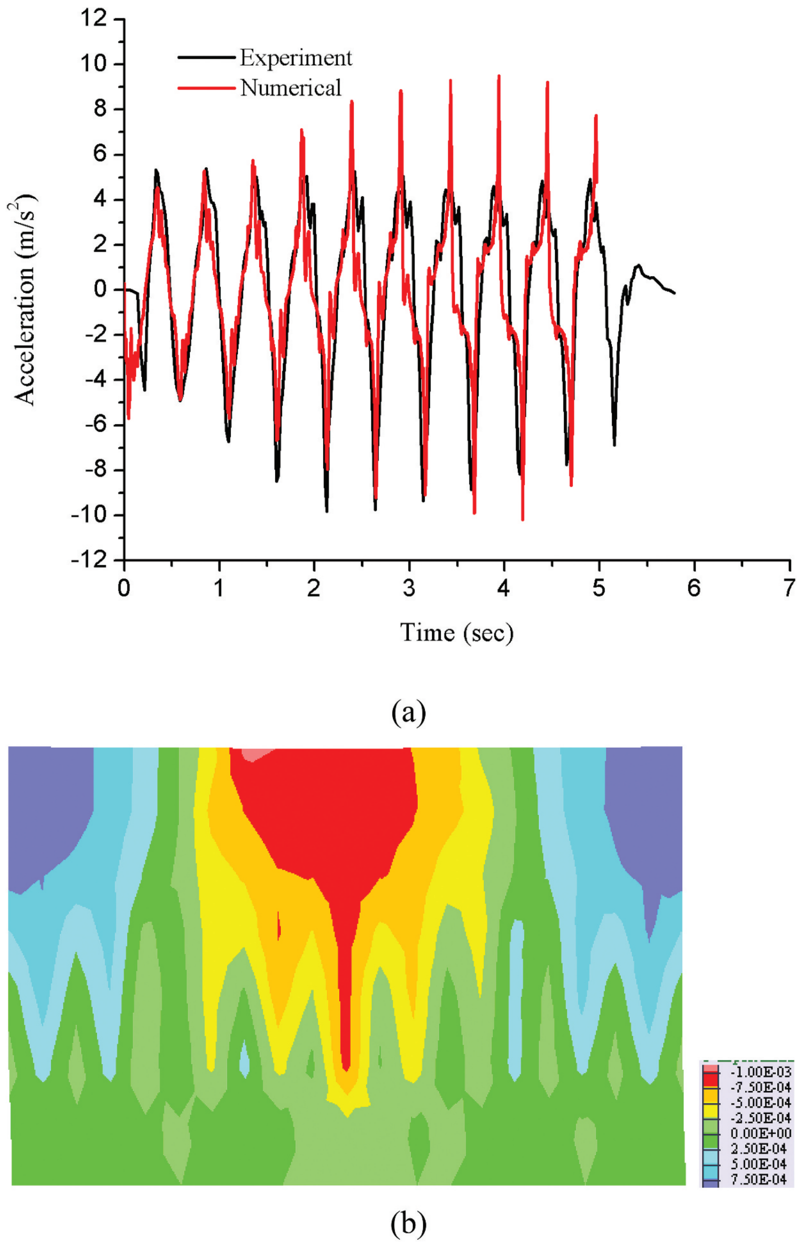

Figure 18. Acceleration responses at the top in (a) time domain and (b) frequency domain.

frequencies of 5 Hz, 8 Hz, and 14 Hz. The corresponding input displacement amplitudes are 0.00355 m, 0.001389 m and 0.000453 m, respectively. The soil properties and the pile dimensions, properties of the pile and the superstructure load are kept same as before and the responses on the piled raft (P1) are studied in terms of PGA amplification or deamplification and the origin of the high-frequency contents on the response spectrum on a piled raft as shown in Figure 22(a).

It is observed in the response spetcrum of the piled raft that as the input motion amplitude gradually increases, the PGA value experienced by the piled raft increases and the origin of the odd harmonics of the input motion becomes predominant. The high-frequency components become more and more significant, the origin of which may be related to the deviation of the stress-strain loops from the conventional elliptical shape and the prominence of sharp corners in the hysteresis loops (Veeraraghavan *et al.* (2019)). This is prominent in the stress-strain loops obtained at 3.5 m below the piled raftand shown in Figure 22(b). Also the PGA amplification/deamplification is related to the strain hardening characteristics, which become prominent when the input amplitude increases (Gang *et al.*

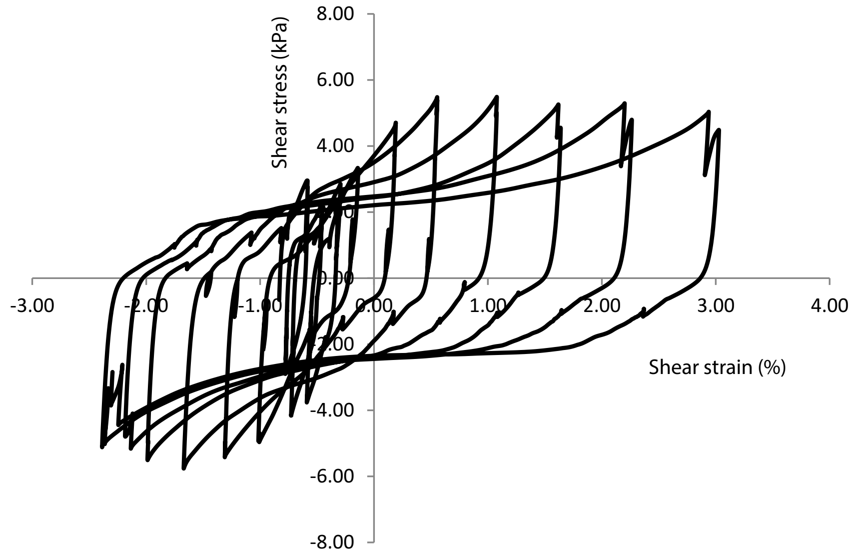

Figure 19. Shear stress-strain loops obtained numerically at a depth of 0.35 m below the piled raft foundation.

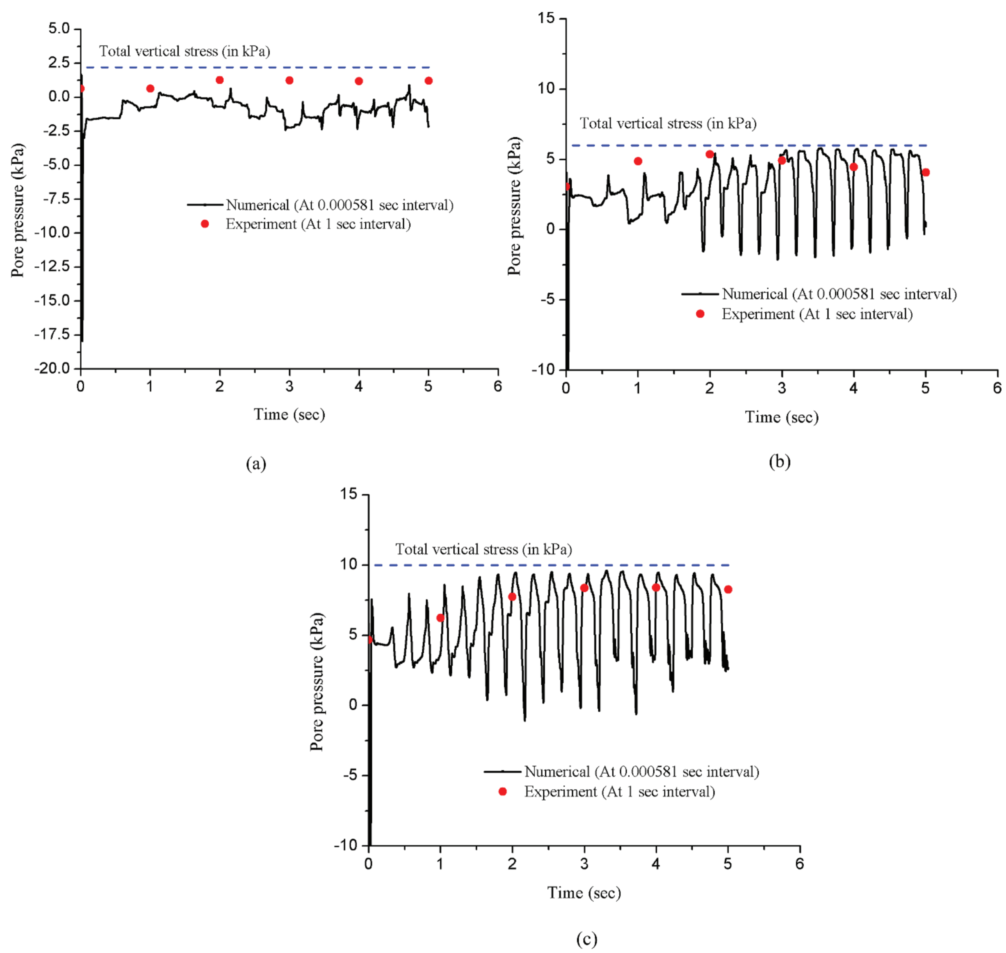

Figure 20. Time history of pore water pressure at (a) top and (b) middle and (c) bottom of the soil foundation.

(2018)). This also gives an idea of the extent to which the soil dilates upon shearing which leads to the amplification of the input motion, except for the first instance when the displacement value is 0.000453 m. When the soil undergoes strain softening and there is significant deamplification of PGA and no presence of high-

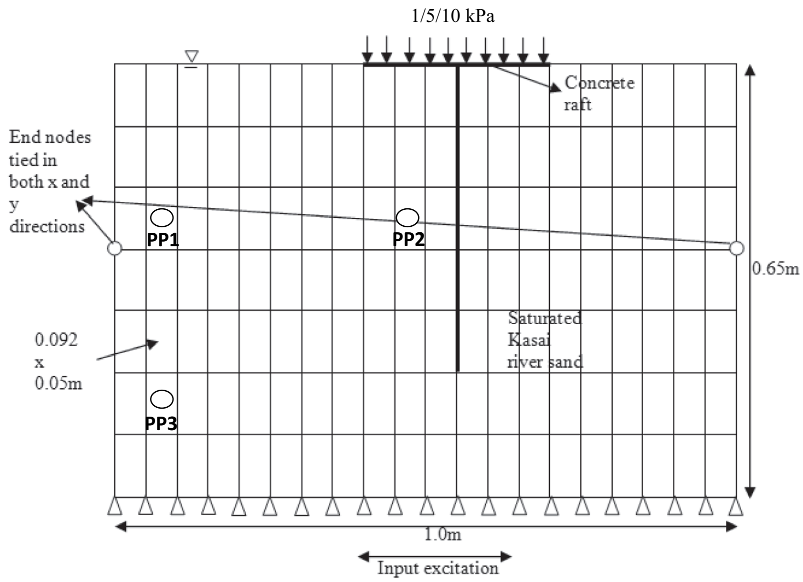

Figure 21. Deformations of the foundation soil at the end of (a) static loading and (b) dynamic loading.

frequency response in the system. This is observed when the input signal frequency is 14 Hz.Thus, the magnitude and frequency of the input motion is found to be a important parameter to be considered for the design of a piled raft under seismic excitation.

7. Effect of superstructure loading on the model piled raft responses

The effect of superstructure loading on a piled raft is studied by subjecting the model to 5 and 10 kPa loads. The input motion(PGA of 0.35 g at 2 Hz for 5 sec), the soil properties and the pile dimensions and properties are kept same as the model test. The analysis is done with no flow condition and no excess pore water pressure dissipation. The locations of pore water pressure gauges in the soil along with all the boundary conditions are shown in Figure 23.

The vertical settlement contours at the end of the dynamic excitation (for loading of 10 kPa vertical loading) is shown in Figure 24. The variation of the vertical settlement of the piled raft (at a distance of 0.05 m and 0.25 m from the left edge of the raft) for two loading values is shown in Figure 25. It is found that for the greater part of the dynamic shaking, the seismic velocities of the raft fluctuate around a more or less constant value, resulting in a linear accumulation of the raft settlement. Table 4 shows the maximum value of the settlement as well as the differential settlement of the raft for different loading values. It is observed that the average and the differential settlements of the raft increase as expected. Hence, from the serviceability point of view, the superstructure load on the piled raft is identified as one of the important parameters under consideration.

The mechanism of shear-induced settlement is very complex. An attempt is made to explain the mechanism of shear-induced vertical settlement (numerically) for a piled raft resting on saturated sand. Dashti *et al.* (2009b) has divided the overall settlement of a foundation into three parts, namely ejecta-induced settlement (in which soil is removed from beneath the foundation and foundation settles), shear-induced settlement and volumetric induced settlement (caused due to the dissipation of excess pore water pressure and reconsolidation after liquefaction). The vertical displacement of a piled raft is found to be not due to the soil densification, rather the piled raft settles when the load on a pile exceeds the yield value. This has been proved by observing the exceedance of the pile capacity and the vertical displacement histories as shown in Figure 26(a,b) (for the case of superstructure loading of 1.0 and 10 kPa). The load near the piled raft head decreases as the soil starts to liquefy. This is due to the loss of the bearing capacity due to seismically induced pore water pressure and the decrease in the base resistance of the pile. The equation proposed by Knappett and Madabhushi (2008) calculates the base resistance of a pile during liquefaction and it is given by

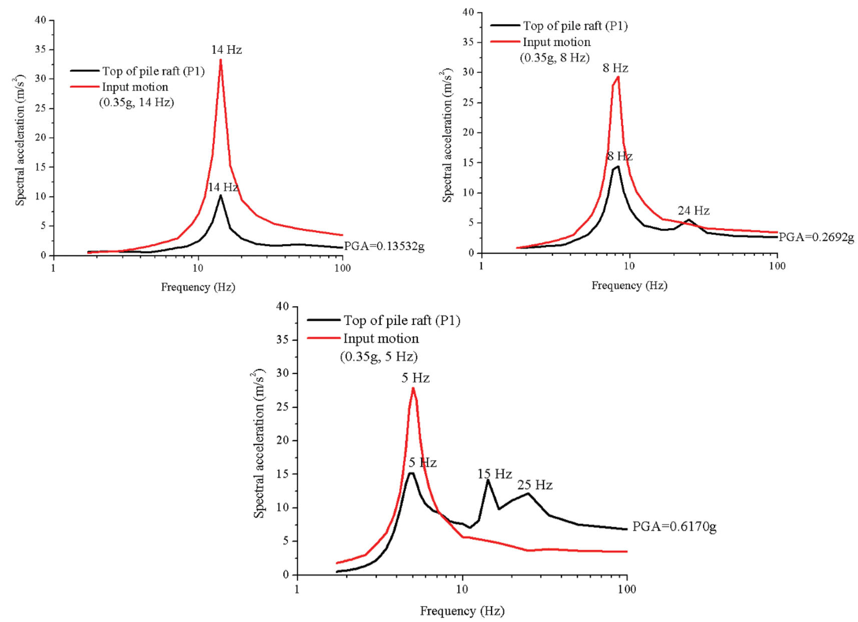

(a)

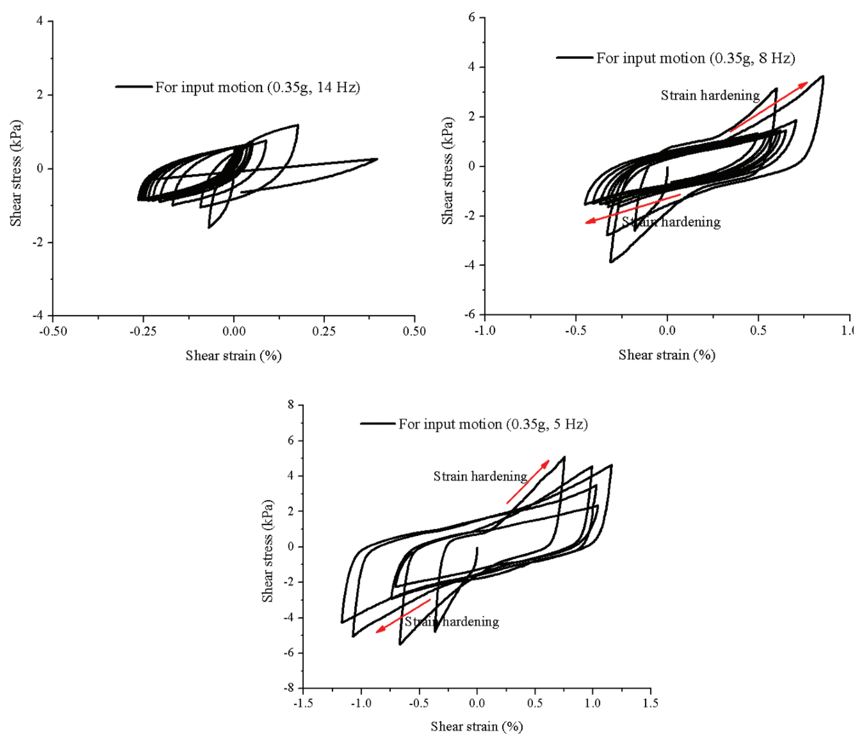

(b)

Figure 22. (a) Response spectrum of piled raft and (b) stress-strain loops of soil at a depth of 3.5 m below the top surface for the 0.35 g motions at 14 Hz, 8 Hz and 5 Hz frequencies.

$$Q_{base} = \sigma_v A \frac{(1+\sin(\varphi))(1+2K_o)}{(1-\sin(\varphi))(3-\sin(\varphi))}\left(\frac{I_r}{(1+I_r\varepsilon)}\right)^{\left(\frac{4\sin\varphi}{3(1+\sin(\varphi))}\right)} \tag{17}$$

in which, $I_r = \frac{3G}{(1+2K_o)\tan(\varphi)\sigma_v}$, where, φ is the angle of internal friction of soil beneath the tip of the pile, A is the base area of the pile, K_o is the coefficient of earth pressure at rest.

During soil liquefaction, both the shear modulus (G) and the instantaneous vertical effective stress (σ_v)

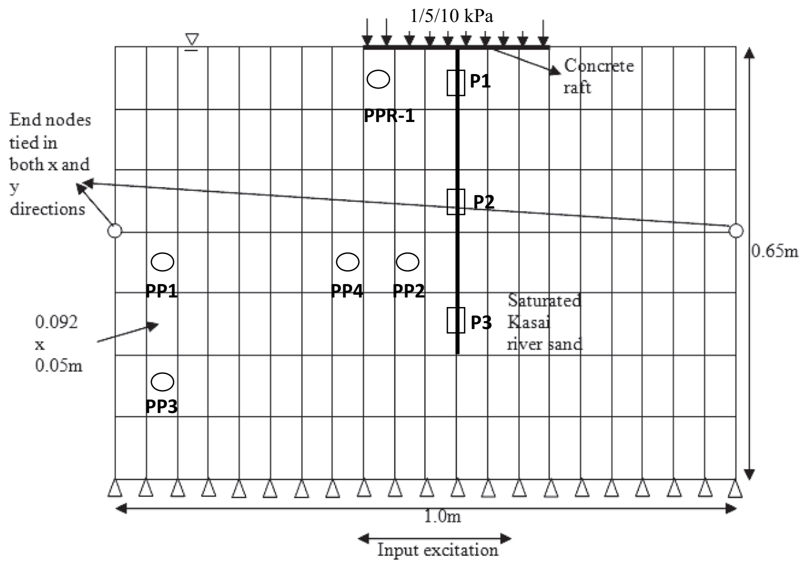

Figure 23. A schematic diagram of the soil and the piled raft along with the measurement locations of pore water pressures.

Figure 24. Vertical settlement contour (in m) at the end of dynamic excitation (for loading of 10 kPa).

reduce as excess pore water pressures increase. The secant values of G for each cycle of the seismic shaking are obtained based on the stress-strain loops of the soil at the mid-way between the tip of the pile and the base of the test tank. Another way is to find the strain time history and corresponding to each strain (absolute value), calculate the value of G/G_{max} from Figure 15. The volumetric compression (ε) is assumed to be zero (undrained). For the skin friction calculation, a conventional method has been followed (as done for static, that is, $f_s A_s = q_o \tan(\varphi) A_s$ where, q_o is the vertical stress, A_s is the surface area of the pile and $\varphi$is the adhesion angle between the soil and the pile (=2/3rd of angle of internal friction of the soil)). The value of the ultimate skin friction (before liquefaction) of the pile is found to be 1.365 N. Despite a significant dynamic component, the average shaft load for the pile steadily reduces as the soil liquefies, which is interpreted as a drop in the shaft capacity of the pile. Hence, a bi-linear fit is defined as below (Knappett and Madabhushi (2008)):

$$\frac{Q_{s\_seismic}}{Q_{s\_static}} = 1, if\ N < 7 \text{ and } -0.014\,\text{N} + 1.1, \text{if N} \geq 7 \tag{18}$$

Where, N is the number of harmonic cycles. In the present case, N = 5, hence $Q_{s\_seismic} = Q_{s\_static}$, hence the skin friction does not change with time and the base resistance is calculated from Equation (17). Adding these two quantities gives the pile capacity with time when soil is undergoing liquefaction. This is subtracted

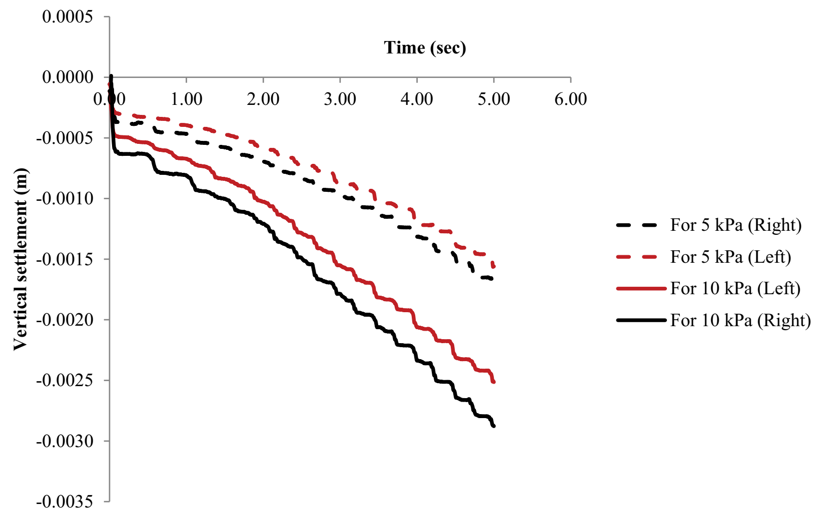

Figure 25. Vertical settlement of the piled raft (at a distance of 0.05 m and 0.25 m from the left edge of raft) for 5 and 10 kPa loadings.

Table 4. Average and differential settlements of the piled raft.

Superstructure loading (kPa)	Average settlement of raft (mm)	Differential Settlement of raft (mm)
5	1.40 mm	0.195 mm
10	2.60 mm	0.385 mm

from the external force on the pile to find out whether the pile capacity (P_{yield}) is exceeded at a certain instant of time as shown in Figure 26(a). If $P_{ext}<P_{yield}$, one will observe a blank zone in Figure 26(a), which indicates that the pile capacity has not exceeded.

From 0 to 1 sec (in the case of 1 kPa loading) in Figure 26(b), it may be observed that the vertical deformation is nearly flat, implying that the pile capacity is not exceeding as observed in Figure 26(a). At the beginning of Figure 26 (a), the pile capacity is exceeded due to which there is a increase in the vertical settlement in both the loading cases. From 3 sec to 5 sec (in the case of 1 kPa loading),

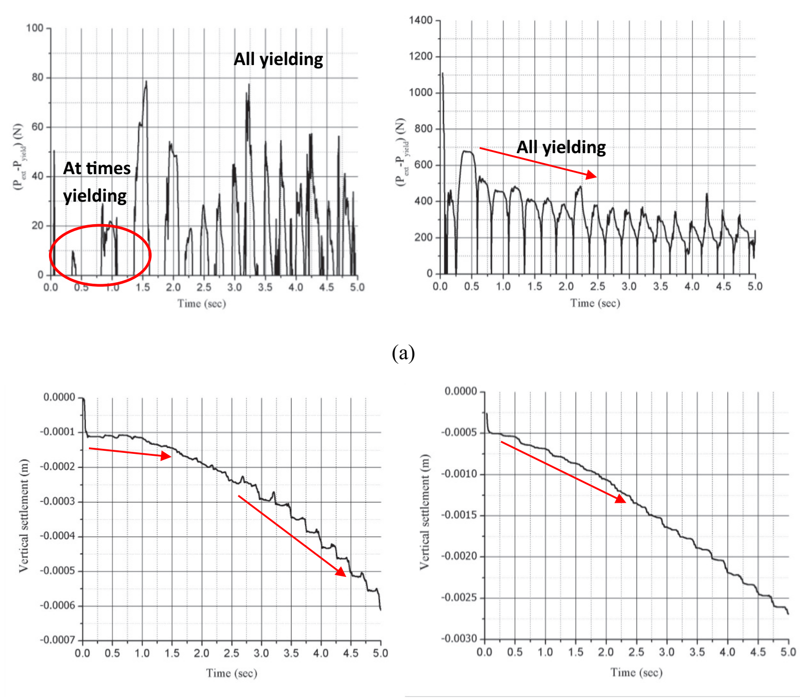

(b)

Figure 26. Vertical deformation with time at which pile capacity is exceeded for (a) 1 kPa and (b) 10 kPa applied on piled raft.

it may be observed that there is no gap between the consecutive peaks, implying that the applied load exceeds the yield load of the pile (that is, the pile capacity is exceeded), hence the piled raft would ‘stamp’ its way into the soil during the motion, with the settlement increasing at a constant rate. This is similar to the accumulation of permanent displacement in a slope during an earthquake when a yield acceleration is exceeded (Newmark 1965). For the case of 10 kPa load, the pile capacity is exceeded all times due to which the piled raft settlement occurs at a constant rate.

Figure 27 shows the responses of the pore water pressure at PP3 for 5 and 10 kPa vertical loadings. It is found that the values of the pore water pressure is not affected by the loading from the superstructure as the point under consideration is far from the influence zone of the piled raft. A similar observation has been reported from the centrifuge tests by Tasiopoulou *et al.* (2013), in which the free field soil liquefied irrespective of the type of structure involved in the tests.

7.1. Influence of piled raft on the variation of pore water pressure responses in the soil

The variation of pore water pressure of free field with respect to that near the piled raft is studied from the effective stress contours of the soil (for the case of 10 kPa loading) at the end of dynamic excitation for 0.35 g at 8 Hz and 14 Hz frequency applied for a duration of 2 seconds. It is observed that there is an area in which the effective stress values are quite high near the foundation, as shown in Figure 28(a,b) at the end of the motion. These zones of large effective stresses near the bottom of the raft (Figure 28(a,b)) indicate the transfer of vertical loads from the pile to the raft after the onset of liquefaction in the form of increased bearing

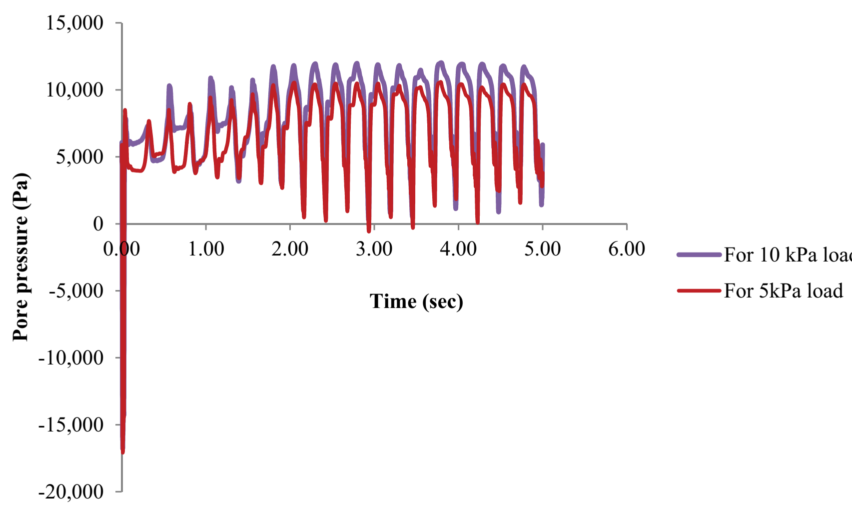

Figure 27. Responses of pore water pressures at PP3 for 5 and 10 kPa vertical loadings.

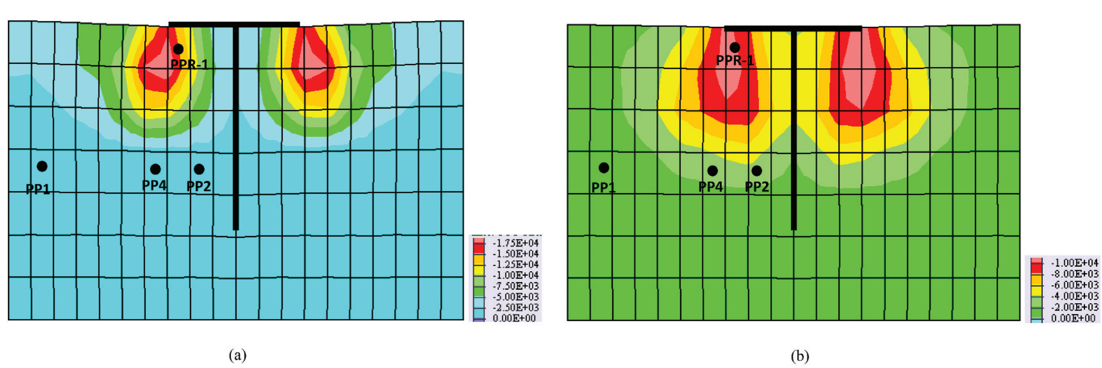

Figure 28. Effective stress contours (in N/m^2) for 10 kPa loading at the end of dynamic loading for 0.35 g motions at (a) 8 Hz and (b) 14 Hz frequency.

pressure under the raft. This is due to the gradual transfer of load from the pile to the raft and it is clear from the time history of the axial pile load at three different locations (P1, P2 and P3) in Figure 29. This is attributed to the significant loss of bearing resistance of the pile (base and shaft resistances of the pile) as explained by Equations (17) and (18) (Knappett and Madabhushi (2008)) due to the complete liquefaction of the soil in the test tank. The pore water pressure below the raft increases above the level of the free field during the initial stage. This increase is related to the decrease in the axial load on the pile. The increase in the vertical stress level in the ground below the raft causes the pore water pressure to rise above the free field level at shallow depths. As the axial load on the pile reaches a threshold value, the pore pressure starts to reduce near the raft bottom (PPR-1) as shown in Figure 30. Before the earthquake, the majority of the load is taken up by the pile. Following the onset of the liquefaction, the load taken by the pile gradually reduces and thus the vertical total and effective stresses beneath the raft increase. A similar phenomenon of load transfer has been observed by Stringer (2011) and Unsever *et al.* (2017) in the centrifuge and 1-g shake table study of piled rafts on saturated sand. Thus, a piled raft has the potential of mitigating liquefaction at shallow depths of the soil as the superstructure load is transferred to the ground at a shallow depth with the

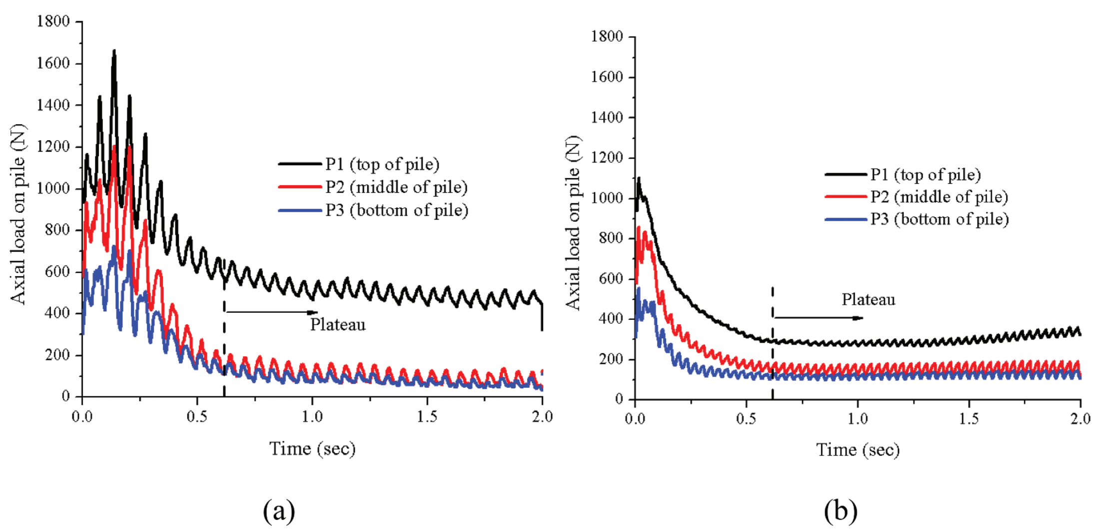

Figure 29. Time history of axial load at three different locations (P1, P2 and P3) on a pile within the piled raft for two motions of (a) 0.35 g, 8 Hz and (b) 0.35 g, 14 Hz.

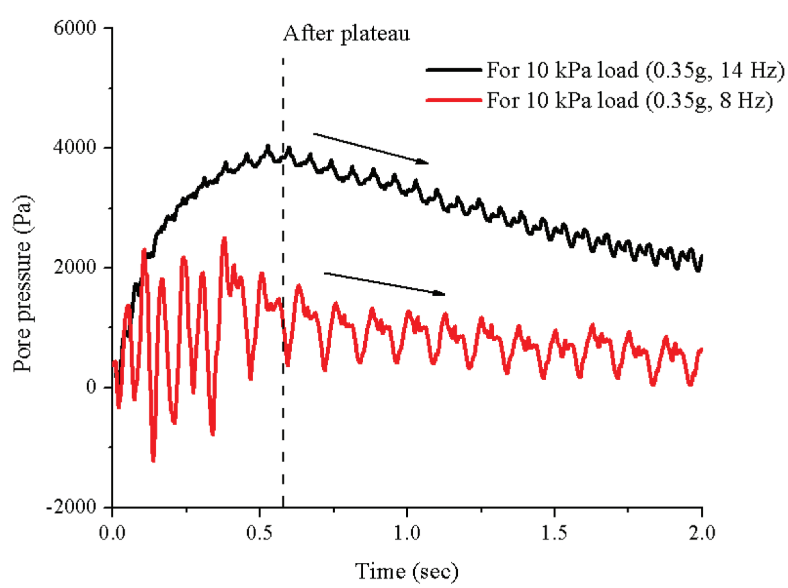

Figure 30. Pore water pressure time history below the raft (PPR-1) for two different motions.

help of the raft in contact with the soil reducing the severity of damage due to the liquefaction.

The effective stress decreases in the horizontal and the vertical directions away from the foundation, which indicates that the soil near the piled raft may liquefy at a much later stage than the free field soil. Figure 31(a,b) shows the variation of pore water pressure from the free field to the structure. It is observed that the rate of pore water pressure increase is slow near the pile (PP4 and PP2) as compared to that at the free field (PP1). It is also observed that the pore water pressure near the pile has a large oscillating (or cyclic) component as compared to that of the free field as may be observed from Figure 31(a,b). This indicates large dilation near the vicinity of the piles. A similar observation has been made experimentally in the centrifuge and the shake table tests by Wang *et al.* (2019), Dash and Bhattacharya (2015) and Tasiopoulou *et al.* (2013). This validates the present outcome of the analysis. The large cyclic component of the pore water pressure originates from the lateral movement of the pile within the saturated soil. When the pile moves towards the point PP2 or PP4, there is a sudden increase of pore water pressure and when it moves away from the points PP2 or PP4, a decrease in the pore water pressure results. As the amplitude of the motion increases, the lateral motion of the piled raft increases due to which the amplitude of oscillation of the pore water pressure increases, hence more dilation is seen in Figure 31(a) as compared to Figure 31(b). This is one of the reasons due to which the maximum value of pore water pressure near the pile becomes a bit less (or equal) to that in the free field (Tasiopoulou *et al.* (2013), Adalier *et al.* (2003)). Adalier *et al.* (2003) have given another explanation which relates to the presence of additional deviator (or static shear) stress induced by the foundation surcharge, which prevents the build-up of pore pressures during shaking. So, the pore water pressure in the free field develops more than that underneath the structure.

Hence, from the 1-g model study conducted on a single-piled raft, the amplitude of the motion and the superstructure load are found to significantly affecting the behaviour of a piled raft and they may be considered as sensitive parameters for the seismic design of a piled raft foundation.

8. Seismic responses of a prototype-piled raft

Based on the identified sensitive design parameters from the model tests, the seismic behaviour of a piled raft is investigated in a prototype scale. The foundation soil domain is 30 m x 13 m in size with a relative density of 52.81% (Figure 9(b)). The horizontal extent of the soil domain has been extended to 30 m (instead of 20 m) to further ensure that the boundary effects are minimised. The depth and the relative density of the saturated soil is the prototype equivalent of the model tests. A 6 m x 6 m x 0.43 m piled raft with 667 mm diameter of pile has been chosen with 3 × 3 pile configuration. Case studies are carried out with all piles of pile length of 7 m and all piles of pile length 10 m.The piled raft is made of M20 grade of concrete with the modulus of elasticity, E = 2.238x10^{10} Pa (using the formulation, $E = 5000\sqrt{f_{ck}}$ (in MPa) as per IS 456 (2000) with Poisson's ratio of 0.15. The piled raft is subjected to two superstructure loads of 28.9 kPa and 57.8 kPa on top of the raft. All the dimensions and properties are also the scaled up values of the models test. As the seismic responses of a piled raft are often

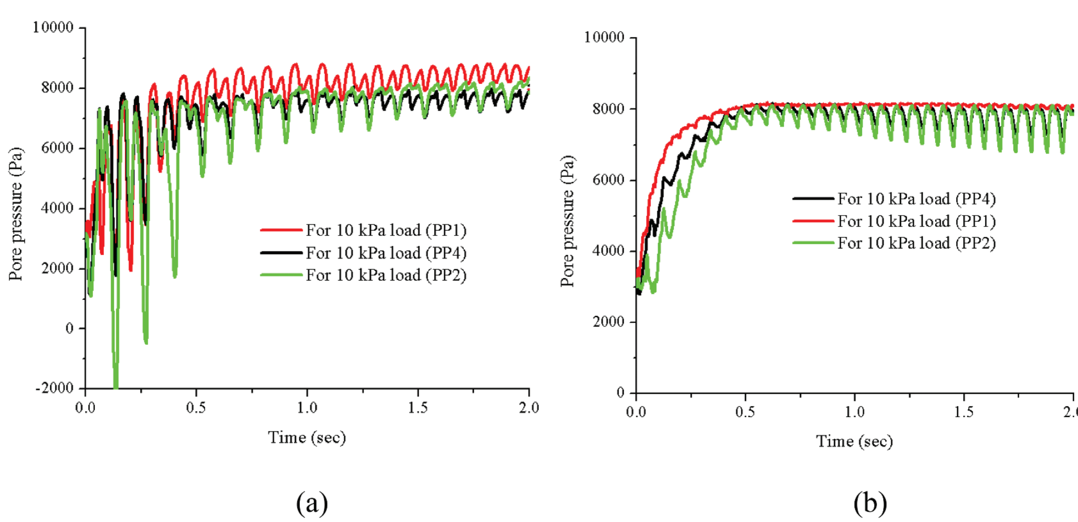

Figure 31. Variation of pore water pressures from free field to the piled raft for 0.35 g at (a) 8 Hz and (b) 14 Hz frequency with 10 kPa superstructure loading.

sensitive to ground motions and soil/structural parameters, hence the parameters used in the present study are summarised in Table 5.

The small strain shear modulus of the soil follows Equation (1) and a coupled dynamic and flow analysis has been performed with the effect of the soil permeability taken into account.The coefficient of the permeability of Kasai River sand is 4×10^{-4} m/s from the correlation proposed by Hazen (1892) for a value of D_{10} of 0.2 mm (from Figure 1). The foundation sand bed (30.0 m in width and 13 m in height) is discretized by 120 × 20 numbers of quadrilateral elements. Each element is of 0.25 m × 0.65 m in size with due considerations given for the maximum frequency (20 Hz) which can propagate through the elements. The soil is modelled by PM4 sand with parameters defined in Table 2. The value of the pore water pressure is fixed at the top surface of the soil throughout the dynamic analysis. A small strain damping (Rayleigh damping) of 2% has been assumed in addition to the hysteretic damping provided by the constitutive model. The value of interaction between the soil, raft and the pile are taken as per Equaiton (15) and explained in the previous section. The out of plane spacing for the piles has been taken to be 2.75 m in this analysis, which is the c/c distance between the piles in the piled raft. The boundary nodes of the model are tied in both the directions during the dynamic analysis. The acceleration-time history is assumed to be acting at the bottom of the soil domain in the numerical analysis. The soil is subjected to various harmonic input motions as listed in Table 5. A plan view of the piled raft and a schematic diagram of the piled raft, soil and the boundary conditions in the numerical analysis are shown in Figure 32(a,b).In order to justify the minimisation of boundary effects, the contours of vertical deformation and the vertical stress contours for the static load of 57.8 kPa are shown in Figure 33(a,b) for 7 m pile. From the vertical stress contours in Figure 33(b), it is observed that, the stresses are free field stress (not influenced by the presence of piled raft) at the boundaries. This also indicates that the boundaries have minimal influence on the formation of stress bulb beneath the piled raft.

Table 5. Sensitive parameters used in the seismic response of piled raft.

Sensitive parameters	
Input motion	
PGA	0.15 g, 0.35 g
Frequency	2, 4, 6, 8 Hz
Duration	5 sec
Superstructure load	
Vertical	28.9, 57.8 kPa
Structure	
Length of pile	7 m, 10 m
Diameter of pile	667 mm
Spacing of pile	2.75 m
Size and thickness of raft	6 m x 6 m x 0.43 m

8.1. Check for serviceability: vertical settlement and angular distortion

The variation of vertical settlements of the piled raft and its angular distortion at the end of the dynamic excitation for different motions are shown in Figure 34(a,b) for 7 m and 10 m pile length. The values are compared with the allowable limits for the vertical settlement and the angular distortion reported by Zhang and Ng (2005) to check for the serviceability of the piled raft. The location at which the vertical settlement is measured is shown in Figure 32(b) and denoted as Point B. The angular distortion is measured as $(V_c\text{-}V_a)/L_{ac}$, where V_a and V_c are the vertical settlements at Points A and C, and L_{ac} is the distance between the two points. From these figures, it is observed that the differential settlement (or angular distortion) is less sensitive to the superstructure load for a given PGA as compared to the total vertical settlement of the piled raft. Also, for a higher PGA, irrespective of the frequency content, the vertical settlement is more sensitive with the change in the superstructure loading. It may be also noted that for longer piles, the vertical settlement reduces irrespective of the amplitude of the motions, but the angular distortion is not affected significantly. Hence, it is recommended to use longer piles to satisfy the serviceability needs of a piled raft in a liquefied soil.

8.2. Check for serviceability: damage to the piles due to seismic excitation

The piles in a piled raft will crack if the bending moment of the pile exceeds the cracking moment at any instant during the seismic excitation. Although all the piles may not crack, but one or more piles may get damaged `during or at the end of a seismic excitation, hence a check is carried out to find out whether the piles may crack or not. The cracking moment of the pile (of circular cross section) is calculated from the expression: $M_{cr} = \frac{f_{cr} I_{gr}}{y_{NA}}$ where, f_{cr} is the flexural strength of the concrete (or modulus of rupture) $=0.7\sqrt{f_{ck}}(in MPa)$ (IS 456 (2000)), f_{ck} is the characteristics strength of the concrete (f_{ck} = 20 MPa for M20 grade of concrete), I_{gr} is the moment of inertia of the pilecross section (ignoring the reinforcements) $(= \pi D^4/64)$ and y_{NA} is the depth of the neutral axis (= D/2), where D is the diameter of the pile (=667 mm). While calculating the cracking moment, it is assumed that the pile section is in elastic

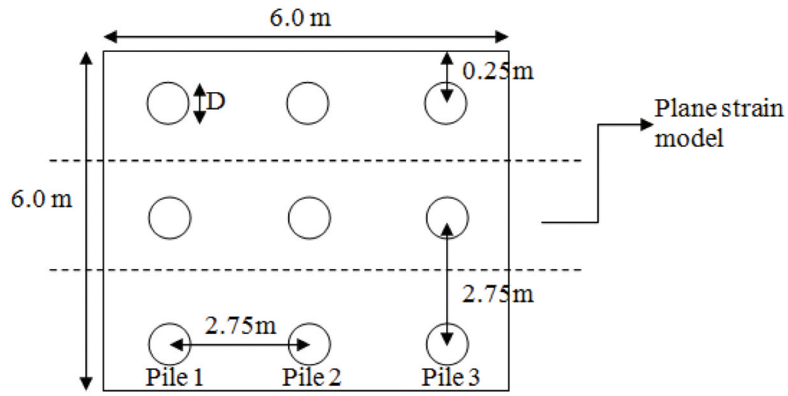

(a)

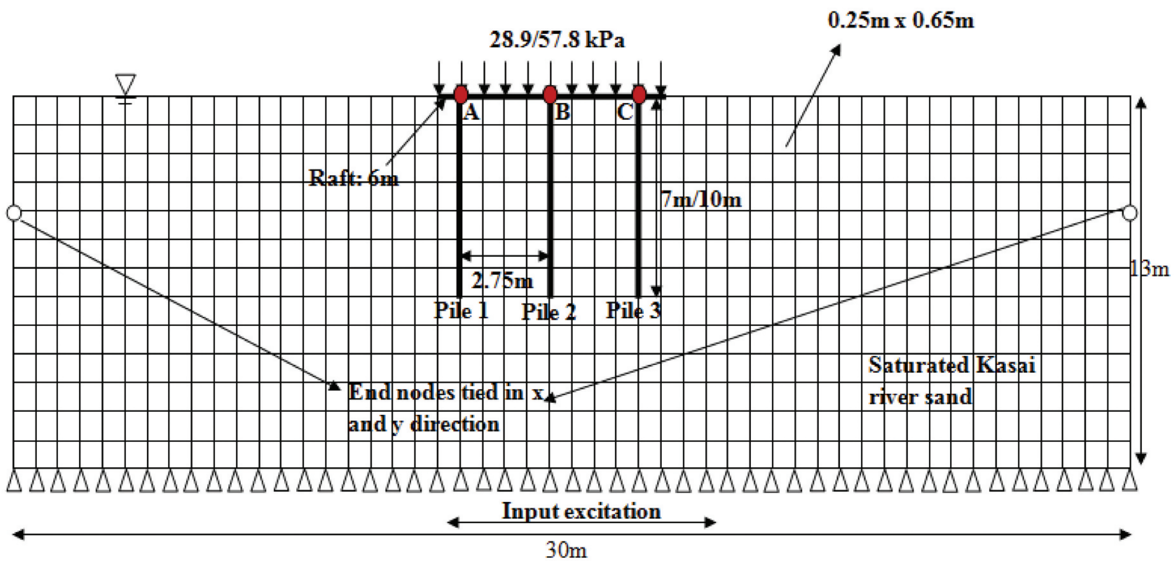

(b)

Figure 32. (a) Plan view of 3 × 3 piled raft and (b) schematic diagram of the soil and the piled raft along with the boundary conditions in the prototype scale.

state or Hooke's law is valid and the cracking moment of the pile section is found to be 92.40 kN-m. Table 6 provides a check for the piles due to cracking for a 7 m pile subjected to superstructure loads of 28.9 kPa and 57.8 kPa.It is observed that the inner piles are less susceptible to cracking than the outer piles for a low amplitude motion (0.15 g with 6 and 8 Hz). For high amplitude motion (0.15 g with 2 and 4 Hz), all the piles are equally susceptible to cracking. The development of cracks indicates the violation of serviceability criteria (as it damages the piles), but it does not include a bending failure of the piles. The piles are cracked near the pile head where the maximum moment is experienced by the pile. A similar type of crack formation has been reported in a case study of Niigata Family Court house, where a floating pile terminating in a loose liquefiable layer cracked near the pile head where it was connected with the foundation beams (Berrill and Yasuda (2002)). It is observed that the various combinations of P_{max}-M_{max} lie below the balanced point of the interaction curve (in tension-controlled region where the concrete is neglected below the neutral axis (tensile zone) and the strain of steel surpasses the yield strain); hence, the contribution of concrete below the neutral axis can be neglected while evaluating the capacity of the pile section.

8.3. Check for strength

As the piles are not embedded into a non-liquefiable soil layer (clay, dense sand or rock) and it is a floating pile, hence the possibility of combined buckling and bending

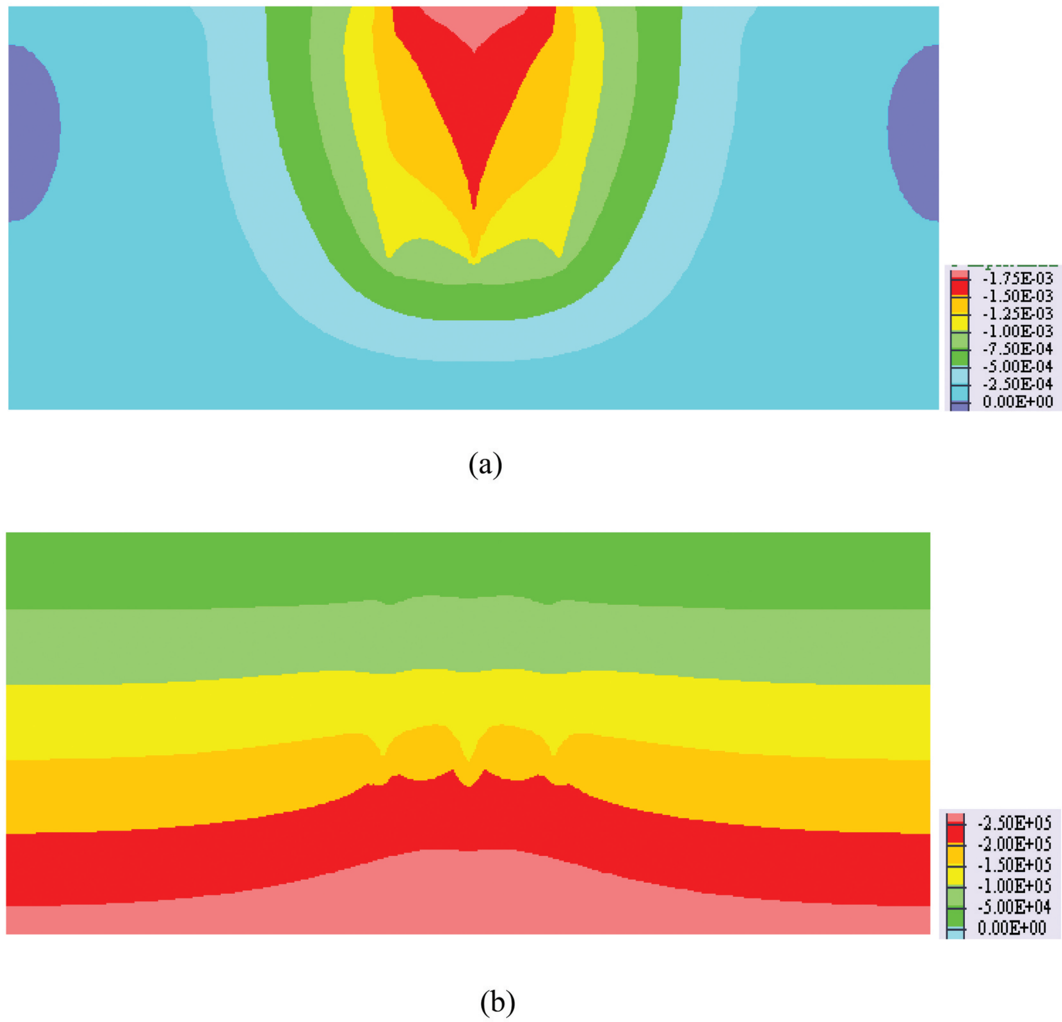

Figure 33. (a) Contours of vertical deformation (in m) and (b) vertical stress (in N/m^2) on the soil with piled raft of 7 m pile length with superstructure load of 57.8 kPa.

failure is eliminated (O'Rourke *et al.* (1994)). In this case, the piles must be checked for thrust and moment, simultaneously. The damaged floating piles of Niigata Family Court house are the piles terminating in the liquefiable layer which were checked for thrust and moment eliminating the possibility of buckling (Berrill and Yasuda (2002)). These piles are subjected to moments due to inertial loads and free field displacements of the liquefiable layer (kinematic interaction) (Berrill and Yasuda (2002)). Assume 1.5% reinforcement (p) in the pile with Fe415 grade of steel and M20 grade of concrete with nominal cover of 50 mm (minimum nominal cover required 40 mm as per IS 456 (2000). It is assumed that the maximum axial force (P_{max}) and the bending moment (M_{max}) experienced by the piles are at the same instant of time and these two values might not be experienced by the same pile, which is a conservative assumption. Hence, from Chart 56 of SP 16 (1980) with d/D = 0.1 and p/f_{ck} = 0.075, the various combinations of P_{max}-M_{max} are plotted in Figure 35 for different motion amplitudes and superstructure loads for a pile length of 10 m. The points lying outside the interaction curve are marked in the figures and are considered unsafe in the strength criteria. These failures are identified by high-level loads with structural capacity exceeding the demand resulting in pile failure near the junction of raft and pile. A similar type of structural failure has been observed after the 1989 Loma Prieta and 1995 Kobe earthquake (Seed *et al.* (1990), Wei *et al.* (2008)).

For a motion of 0.15 g at 4 Hz with a superstructure load of 57.8 kPa and pile length of 10 m (Point A in Figure 35), the value of maximum axial force (P_{max}) and the bending moment (M_{max}) are found from the effective stress analysis as 521.005 kN and 284 kN-m. The value of $P_{max}/f_{ck}D^2$ and $M_{max}/f_{ck}D^3$ are 0.058 and 0.0472, respectively, and the value of p/f_{ck} is 0.03 (from Chart 56 of SP 16 (1980)). Hence, the required percentage of steel (p_{red}) is 0.03 × 20 = 0.6%, which is less than 1.5%. Hence the pile section is safe and the point lies inside the interaction curve.

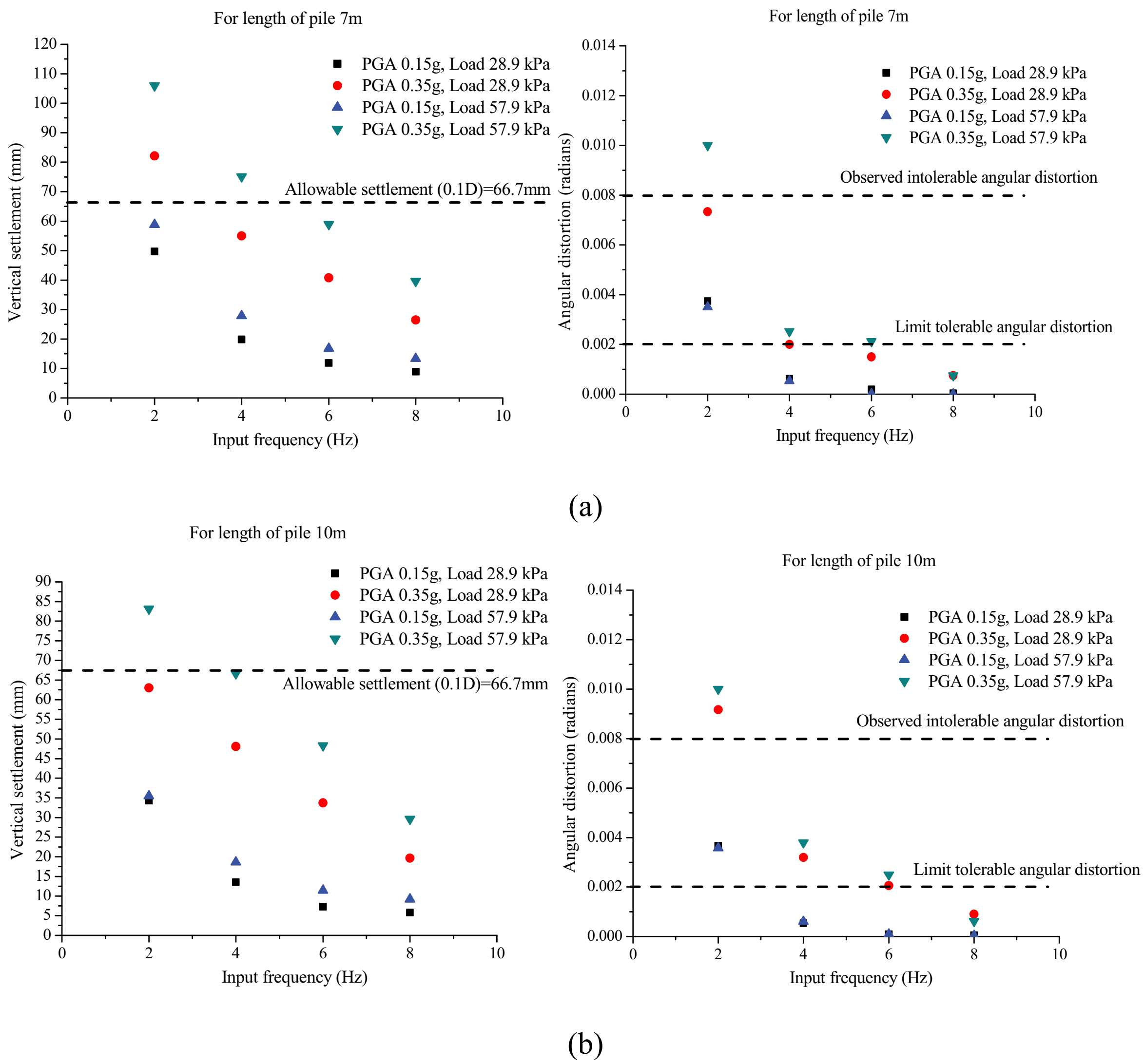

Figure 34. Variation of vertical settlement and angular distortion for different motions and loads for pile length of (a) 7 m and (b) 10 m.

Table 6. Checking of cracks in a piled raft.

Input motion	M_{max} (Pile 1)	Comments	M_{max} (Pile 2)	Comments	M_{max} (Pile 3)	Comments
Cracking moment 92.4 kN-m (Pile length 7 m,Load 57.8 kPa)						
0.15 g, 2 Hz	368	Crack	500.563	Crack	364	Crack
0.15 g, 4 Hz	220	Crack	186	Crack	182	Crack
0.15 g, 6 Hz	186	Crack	88.98	**No crack**	158	Crack
0.15 g, 8 Hz	176.16	Crack	52.104	**No crack**	157.96	Crack
Cracking moment 92.4 kN-m (Pile length 7 m,Load 28.9 kPa)						
0.15 g, 2 Hz	307.24	Crack	438.20	Crack	369.24	Crack
0.15 g, 4 Hz	185.45	Crack	90	**No crack**	182.5	Crack
0.15 g, 6 Hz	137.05	Crack	86.6	**No crack**	109.98	Crack
0.15 g, 8 Hz	121.682	Crack	55.903	**No crack**	99.875	Crack

When the piled raft is subjected to a large motion (0.15 g, 0.35 g at 2 Hz), the risk of liquefaction increases and the probability of violating the serviceability criteria and failure of the pile increase as may be seen from the interaction plot. But in case of other motions, the piled raft is safe. Hence, it is concluded that the parameters chosen are quite sensitive to the design of piled raft foundation. The variation of maximum bending moment and the shear force acting on the pile for different PGA sand for a pile length of 7 m with superstructure load of 57.8 kPa are shown in Table 7. It may be noted that the bending moment and the shear force

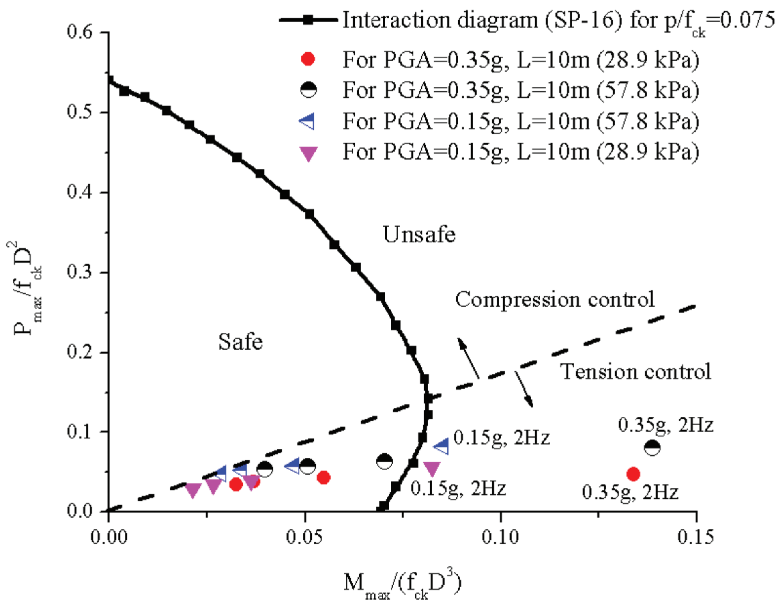

Figure 35. Interaction diagram of thrust and moment for a circular RC section with p/f_{ck} = 0.075.

Table 7. Effect of PGA on bending moment and shear force in the piles.

PGA	0.35 g	0.15 g	0.35 g	0.15 g
Frequency (Hz)	M_{max} (kN-m)	M_{max} (kN-m)	V_{max} (kN)	V_{max} (kN)
2	570.881	500	178	103.382
4	319.163	228.603	132.79	89.98
6	280.502	186.386	123.984	75.087
8	226.388	176.163	99.882	65.336

acting on the pile head are more when the value of PGA increases with the frequency remaining constant. This also implies the importance of the effect of PGA on the failure of a pile.

9. Conclusions

A proper calibration of cyclic triaxial tests along with the validation of shake table test have been performed. The numerical results are in good agreement with the experimental observations. In addition, the effect of loading on a model piled raft response has been investigated in terms of pore water pressure and vertical settlement of a piled raft.

As the shake table test has been conducted in a 1-g environment and at a low-confining stress with a large displacement (=0.022 m), the entire soil mass undergoes extensive dilation. Although the prototype soil have the same relative state parameter (ξ_R) as that of the model to ensure the similar stress paths, but the extent of dilation in the prototype soil is found to be not matching with that in the test. Also, due to the rigidity of the side walls of the test tank, the boundary effects cannot be completely avoided in the shake table tests even with the recommended 32 mm thermocol pads in place along the side walls.

It is also observed that the maximum pore water pressure value is less near the piles under the raft as compared to that in the free field. The extent of oscillation of pore water pressure near the pile is much more compared to the free field value and the rate of increase of pore pressure is also less in comparison to that in the free field. It is also noted that the pile sheds load to the raft during the dynamic excitation due to the gradual loss in bearing capacity of the pile and this results in an increased bearing pressure for the raft. The mechanism of vertical settlement of model piled raft is found to be related to the bearing capacity failure of the pile and not on the soil densification.

As the frequency of excitation decreases the high-frequency components (odd harmonics of the input motion) are obtained at the raft (refer Figure 22), the corresponding PGA value on the raft also increases.

In the present study, the numerical results of the prototype piled raft are utilised to come up with a simplified design (serviceability and strength) criterion which incorporates the interaction of thrust and bending in piles. The possibility of bending and buckling in piles are ruled out under the present circumstance. The serviceability check of a piled raft not only should include a check for allowable settlement or angular distortion, but also needs to include a check for a bending crack formation in piles at the location of maximum moment in the piles.

It is also to be noted that the maximum bending moment and the shear force acting on the pile head are a function of both PGA and input frequency and the value increases when the PGA value increase with the frequency remaining constant and for a given PGA the input frequency decreasing.

Disclosure statement

No potential conflict of interest was reported by the author(s).

ORCID

Raj Banerjee http://orcid.org/0000-0002-0359-5738

References

Adalier, K., *et al.*, 2003. Stone columns as liquefaction counter measure in non-plastic silty soils. *Soil Dynamics and Earthquake Engineering*, 23 (7), 571–584. doi:10.1016/S0267-7261(03)00070-8

Amini, F. and Qi, G., 2000. Liquefaction testing of stratified silty sands. *Journal of Geotechnical and Geoenvironmental Engineering*, 126, 208–217. doi:10.1061/(ASCE)1090-0241(2000)126:3(208)

ASTM standard D5311, 2011. *Test method for load controlled cyclic triaxial strength of soil*. Annual book of ASTM standards, ASTM International West Conhohocken PA.

Banerjee, R., *et al.*, 2017. Shake table tests and numerical modeling of Kasai River Sand. *Geotechnical and Geological Engineering*, 35 (4), 1327–1340. doi:10.1007/s10706-017-0178-z

Banerjee, R., Sengupta, A., and Reddy, G.R., 2019. Study of a surface raft foundation in dry cohesionless soil subjected to dynamic loading. *Current Science*, 117 (11), 1800–1812. doi:10.18520/cs/v117/i11/1800-1812

Berrill, J. and Yasuda, S., 2002. Liquefaction and piled foundations: some issues. *Journal of Earthquake Engineering*, 6 (1), 1–41. doi:10.1080/13632460209350431

Bolton, M.D., 1986. The strength and dilatancy of sands. *Géotechnique*, 36, 65–78. doi:10.1680/geot.1986.36.1.65

Boulanger, R.W., Kamai, R., and Ziotopoulou, K., 2011. Numerical modeling of liquefaction effects. *In*: *Proc., Effects of Surface Geology on Seismic Motion, 4th IASPEI/IAEE International Symposium*, Santa Barbara, CA: University of California.

Boulanger, R.W. and Ziotopoulou, K., 2015. PM4 sand (Version 3): a sand plasticity based model for earthquake engineering applications, Report No. UCD/CGM-15/01. Centre for Geotechnical Modeling, Dept. of Civil and Environmental Engg. University of California Davis, CA.

Budhu, M., 2011. *Soil mechanics and foundation*. 3rd ed. Hoboken: John Wiley & Sons, Inc.

Byrne, P.M., *et al.*, 2004. Numerical modeling of liquefaction and comparison with centrifuge tests. *Canadian Geotechnical Journal*, 41, 193–211. doi:10.1139/t03-088

Chattaraj, R. and Sengupta, A., 2016. Liquefaction potential and strain dependent dynamic properties of Kasai River sand. *Soil Dynamics and Earthquake Engineering*, 90, 467–475. doi:10.1016/j.soildyn.2016.07.023

Dafalias, Y.F. and Manzari, M.T., 2004. Simple plasticity sand model accounting for fabric change effects. *Journal of Engineering Mechanics, ASCE*, 130 (6), 622–634. doi:10.1061/(ASCE)0733-9399(2004)130:6(622)

Dasgupta, S., *et al.*, 2000. *Seismotectonic Atlas of India and its environs*. Kolkata, India: Geological Society of India.

Dash, S.R. and Bhattacharya, S., 2015. Pore water pressure generation and dissipation near to pile and far-field in liquefiable soils. *International Journal of GEOMATE*, 9 (2), 1454–1459.

Dashti, S., *et al.*, 2009a. Centrifuge testing to evaluate and mitigate liquefaction-induced building settlement mechanisms. *Journal of Geotechnical & Geoenvironmental Engineering ASCE*, 13, 918–929.

Dashti, S., *et al.*, 2009b. Mechanisms of seismically induced settlement of buildings with shallow foundations on liquefiable soil. *Journal of Geotechnical and Geoenvironmental Engineering*, 136, 151–164. doi:10.1061/(ASCE)GT.1943-5606.0000179

Erten, D. and Maher, M., 1995. Liquefaction potential of silty soils. *Soil Dynamics and Earthquake Engineering*, 14, 115–123. doi:10.1016/0267-7261(94)00035-F

Fallahzadeh, M., *et al.*, 2019. Seismic performance of end-bearing piled raft with countermeasure strategy against liquefaction using centrifuge model tests. *Bulletin of Earthquake Engineering*, 17, 5929–5961. doi:10.1007/s10518-019-00696-z

Gang, W., Xing, W., and Zhao, J., 2018. Modelling spiky acceleration response of dilative sand deposits during earthquakes with emphasis on large post-liquefaction deformation. *Earthquake Engineering and Engineering Vibration*, 17, 125–138. doi:10.1007/s11803-018-0429-x

Hazen, A., 1892. Some physical properties of sand and gravels, with special reference to their use in filtration. *In*: *24th Annual Report Massachusetts State Board of Health*, 34, 539–556. Harvard University Press.

Horikoshi, K., *et al.*, 2003b. Performance of piled raft foundations subjected to static horizontal loads. *International Journal of Physical Modeling in Geotechnics*, 3 (2), 37–50.

Hushmand, B., Scott, R., and Crouse, C., 1988. Centrifuge liquefaction tests in a laminar box. *Geotechnique*, 38 (2), 253–262. doi:10.1680/geot.1988.38.2.253

Iai, S., 1989. Similitude for shaking table tests on soil-structure-fluid model in 1g gravitational field. *Soils and Foundations*, 29 (1), 105–118. doi:10.3208/sandf1972.29.105

Idriss, I.M. and Boulanger, R.W., 2008. *Soil liquefaction during earthquakes (Monograph MNO- 12)*. Oakland, CA: Earthquake Engineering Research Institute, 261.

IS 1893, 2002. *Indian Standard criteria for earthquake resistant design of structures, Part 1 – general provisions and buildings*. Fifth Revision ed. New Delhi: Bureau of Indian Standards.

IS 456, 2000. *Indian standard plain and reinforced concrete code of practice*. New Delhi: Bureau of Indian Standards.

Itasca, 2005. *User's guide for FLAC version 5.0*. India: Itasca India Consulting, Nagpur.

Knappett, J. and Madabhushi, G., 2008. Mechanism of pile group settlement in liquefiable soils. *Geotechnical Earthquake and Engineering and Soil Dynamics IV Congress*. Sacramento, CA.

Knappett, J. and Madabhushi, G., 2009a. Influence of axial load on lateral pile response in liquefiable soils. *Physical Modeling of Geotechnical*, 59 (7), 571–581.

Knappett, J. and Madabhushi, G., 2009b. Seismic bearing capacity of piles in liquefiable soils. *Soils and Foundations*, 49 (4), 525–535. doi:10.3208/sandf.49.525

Manzari, M.T. and Dafalias, Y.F., 1997. A critical state two-surface plasticity model for sand. *Géotechnique*, 47 (2), 255–272. doi:10.1680/geot.1997.47.2.255

Menq, F.Y., 2003. Dynamic properties of sandy and gravelly soils. Ph D dissertation. University of Texas.

Mittal, R.K., Gupta, M.K., and Singh, S., 2004. Liquefaction behaviour of sand during vibrations. *In*: *Proceedings ofthe 13th World Conference on Earthquake Engineering*, Vancouver, B.C., Canada.

Mullins, J.P., *et al.*, 1977. Effects of sample preparation on sand liquefaction. *Journal of Geotechnical Engineering Division*, 10 (2), 91–108.

Nakai. 2004. Load bearing mechanism of piled raft foundation during earthquake. *Proceedings of 3rd UJNR Workshop on Soil Structure Interaction*, 29–30 March, California.

Newmark, N.M., 1965. Effects of earthquakes on dams and embankments. *Géotechnique*, 15 (2), 139–160. doi:10.1680/geot.1965.15.2.139

O'Rourke, T.D., *et al.*, 1994. Evaluation of pile response to liquefaction induced lateral spread, Technical Report NCEER-94–0026. Buffalo, NY: NCEER, 457–479.

Polito, C.P. and Martin, J.R., II, 2001. Effects of nonplastic fines on the liquefaction resistance of sands. *Journal of Geotechnical and Geoenvironmental Engineering*, 127, 408–415. doi:10.1061/(ASCE)1090-0241(2001)127:5(408)

Ravaska, O., 2006. Effect of testing conditions on the shear strength parameters-a numerical study. *In*: *Proceedings of the Sixth International Conference on Numerical Methods in Geotechnical Engineering*, Graz Austria, 161–165.

Roscoe, K.H. and Poorooshasb, H.B., 1963. A fundamental principle of similarity in model tests for earth pressure problems. *In*: *Proc. 2nd Asian Conf. Soil Mech*., Tokyo, 1, 134.

Sahraeian, S.M.S., Takemura, J., and Seki, S., 2017. Centrifuge model study on the effects of pile installation process on seismic behavior of piled raft foundation for oil storage tanks. *Journal of JSCE*, 5(1), 357–376.

Sahraeian, S.M.S., Takemura, J., and Seki, S., 2018. An investigation about seismic behavior of piled raft foundation for oil storage tanks using centrifuge modelling. *Soil Dynamics and Earthquake Engineering*, 104, 210–227.

Salgado, R., Bandini, P., and Karim, A., 2000. Shear strength and stiffness of silty sand. *Journal of Geotechnical and Geoenvironmental Engineering*, 126, 451–462. doi:10.1061/(ASCE)1090-0241(2000)126:5(451)

Seed, H.B., *et al.*, 1975. Representation of irregular stress time histories by equivalent uniform stress series in liquefaction analysis. *In*: *EERC-75–29*, Berkeley: University of California.

Seed, R., *et al.* 1990. Preliminary report on the principal geotechnical aspects of the October 17, 1989 Loma Prieta earthquake. *In*: *UCB/EERC-90/05*, Berkeley: University of California.

SP 16, 1980. Design aids for reinforced concrete to IS 456:1978.[CED 2: cement and concrete]. New Delhi: Bureau of Indian Standards.

Stringer, M., 2011. The axial behavior of piled foundations in liquefiable soil. Dissertation (PhD). University of Cambridge, UK.

Stringer, M. and Madabhushi, G., 2013a. Axial load transfer in liquefiable soils for free-standing piles. *Geotechnique*, 63 (5), 400–409. doi:10.1680/geot.11.P.078

Stringer, M. and Madabhushi, G., 2013b. Re-mobilisation of pile shaft friction after an earthquake. *Canadian Geotechnical Journal*, 50 (9), 979–988. doi:10.1139/cgj-2012-0261

Tasiopoulou, P., *et al.*, 2013. Pile-group response to large soil displacements and liquefaction: centrifuge experiments versus a physically simplified analysis. *Journal of Geotechnical and Geoenvironmental Engineering. ASCE*, 139 (2), 223–233. doi:10.1061/(ASCE)GT.1943-5606.0000759

Thevanayagam, S. and Martin, G., 2002. Liquefaction in silty soils-screening and remediation issues. *Soil Dynamics and Earthquake Engineering*, 22, 1035–1042. doi:10.1016/S0267-7261(02)00128-8

Ueng, T.S., *et al.*, 2005. A large biaxial shear box for shaking table test on satuated sand. *Geotechnical Testing Journal*, 29 (1), 1–8.

Unsever, Y.S., *et al.*, 2017. Behaviour of model pile foundations under dynamic loads in saturated sand. *Bulletin of Earthquake Engineering*, 15, 1355–1373. doi:10.1007/s10518-016-0029-y

Veeraraghavan, S., Spears, R.E., and Coleman, J.L., 2019. High frequency content in nonlinear soil response: anumerical artifact or a reality? *Soil Dynamics and Earthquake Engineering*, 116, 185–191. doi:10.1016/j.soildyn.2018.09.044

Wang, X., *et al.*, 2019. Shake-table investigation of scoured RC pile-group-supported bridges in liquefiable and nonliquefiable soils. *Earthquake Engineering & Structural Dynamics*, 48 (11), 1217–1237. doi:10.1002/eqe.3186

Wei, X., Wang, Q.Q., and Wang, J.J., 2008. Damage patterns and failure mechanisms of bridge pile foundation under earthquake. *In*: *The 14th World Conference on earthquake Engineering*. Beijing, China.

Wood, D.M., 2004. *Geotechnical modeling*. London, UK: CRC Press.

Xenaki, V.C. and Athanasopoulos, G.A., 2003. Liquefaction resistance of sand-mixtures: an experimental investigation of the effect of fines. *Soil Dynamics and Earthquake Engineering*, 23, 183–194. doi:10.1016/S0267-7261(02)00210-5

Yamamuro, J.A. and Covert, K.M., 2001. Monotonic and cyclic liquefaction of very loose sands with high silt content. *Journal of Geotechnical and Geoenvironmental Engineering*, 127, 314–324. doi:10.1061/(ASCE)1090-0241(2001)127:4(314)

Zeghal, M. and Elgamal, A.W., 1994. Analysis of site liquefaction using earthquake records. *Journal of Geotechnical Engineering, ASCE*., 120(6), 996–1017.

Zhang, L. and Ng, A., 2005. Probabilistic limiting tolerable displacements for serviceability limit state design of foundations. *Geotechnique*, 55, 151–161. doi:10.1680/geot.2005.55.2.151